BNL-228370-2025-JAAM

Promoting the oxidative coupling of methanol and dimethylamine using group 1 alkali metals on palladium-gold nanoparticles

A. Minne, E. Stavitski

To be published in "Applied Catalysis B: Environment and Energy"

December 2025

Photon Sciences

Brookhaven National Laboratory

U.S. Department of Energy

USDOE Office of Science (SC), Basic Energy Sciences (BES). Scientific User Facilities (SUF)

DISCLAIMER

Promoting the Oxidative Coupling of Methanol and Dimethylamine using Group 1 Alkali Metals on Palladium-Gold Nanoparticles

Alexander P. Minne[1], Treycen D. Garton[1], Ethan P. Iaia[1], Eli Stavitski,[2] and James W. Harris[1]

[1]Department of Chemical and Biological Engineering, The University of Alabama, Tuscaloosa, AL, 35487
[2] National Synchrotron Light Source II, Brookhaven National Laboratory, Upton, New York 11973, United States

Abstract

$PdAu/SiO_2$ catalysts are synthesized by strong electrostatic adsorption (SEA) and characterized by TEM, DRIFTS, XRD, XAS, and O_2-TPD. The usage of group 1 alkali salt solutions to control SEA synthesis pH leads to uptake of alkali metals observed by caping of terminal silanol groups of the SiO_2 support. In absence of alkali metals 1:5 $PdAu/SiO_2$ catalyzes oxidative C-N bond formation between methanol and DMA, yielding DMF with ~95% carbon selectivity (CO_2 ~5%) below 413 K. When Na, K, and Cs are present on the catalyst, methyl formate (MF) and tetramethylurea (TMU) are observed as additional products (combined ~30% carbon selectivity) while only MF is detected with Li. Total coupling product rate increased for promoted samples in the order Li < Na < Cs < K, and the apparent kinetics over a Cs promoted sample revealed changes including suppression of DMA and methanol orders and a lack of changes to the apparent O_2 reaction order. This work demonstrates the sensitivity of oxidative coupling reactions to alkali metal promoters.

Keywords: Oxidative, Coupling, Bimetallic, Alkali, Promoter, Gold, Palladium
*To whom all correspondence should be addressed, e-mail: james.harris@eng.ua.edu

1. Introduction

Supported PdAu alloy catalysts have been documented for oxidative self-coupling of methanol [1-4]. Our previous publications expand oxidative coupling to the selective cross-coupling of methanol and dimethylamine (DMA) [5, 6]. The role of inorganic promoters (e.g. alkali metals) in oxidative coupling over bimetallic catalysts has not been explored to our knowledge while alkali metals have been used widely in the chemical industry to promote (and poison) reactions [7]. For example, potassium promotes structural and electronic effects in iron catalysts for ammonia synthesis by increasing the low coverage N_2 sticking coefficient significantly as a result of an increase in the binding of the molecular state, reduction in the barrier to dissociation, and enhancement of the adsorption rate of N_2 [7]. Raje et al. [8] reported a complex network of potassium acting as Fischer-Tropsch synthesis (FTS) poison and water-gas-shift (WGS) promoter on iron-silica catalysts. At low CO conversions, K acts as a poison and hampers the rate of FTS by increasing CO surface adsorption. At intermediate CO conversions, K promotes hydrogen production via WGS which supplements hydrogen in the reactor for the FTS reaction [8]. Nakamura et al. [9] reported that cesium influences the kinetics of WGS on model Cu(110) and Cu(111) by acting as an oxygen adatom stabilizer and forming surface carbonate complexes ($CsCO_3$). Thus, CO proceeds along the WGS pathway via unique CsO surface species not present on Cs-free Cu single crystal surfaces [9].

Recognizing the importance of alkali promoted catalysts in the chemical industry and understanding how alkali metals interact with catalysts prepared by strong electrostatic adsorption (SEA) is critical, as alkali hydroxides (e.g., NaOH) are often reported for controlling pH during SEA [10-15]. Currently, there is a lack of studies focused on alkali metal uptake during the SEA synthesis process, although uptake of positively charged alkali ions to a deprotonated silica surface in basic media would be expected. Schreier and Regalbuto [16] recorded sodium uptake in high pH ranges on fumed silica and precipitated silica by sodium ICP (inductively coupled plasma-optical emission spectroscopy) [16]. While fumed silica had little to no uptake of Na^+ in the pH range 10-13.5, precipitated silica exhibited some Na^+ uptake in the same pH range. These conflicting results were not investigated further (to our knowledge), though uncertainty in ICP data for Na content (commonly observed due to Na content in solvents and acids used for sample digestion) was suggested to be a contributing factor [16].

Alkali metals have been described as electropositive promoters of oxidation reactions that improve the chemisorption of electron acceptor adsorbates (molecules that accept electrons from a surface) and diminish the chemisorption of electron donor adsorbates (molecules that donate electrons from a surface) [17]. The mechanism of the alkali-metal promotion on activation of diatomic molecules on transition metals is the weakening of the diatomic bonds which stems from the electron enrichment of the metal phase and increased basic strength of the surface due to the presence of the alkali-metals [18]. Examples of alkali promotional effects have been previously observed in the weakening of C-O and N-O bonds [19, 20] as well as in the enhanced performance of platinum and rhodium catalysts in preferential oxidation of CO in hydrogen rich streams allowing for higher conversion at lower temperatures [21]. Alkali metals also have low (2-3 eV) work functions [22-24] and low ionization potentials. The adsorption of alkali metals on both transition and free-electron metals (e.g., Al) is accompanied by distinctive changes in the work function of the metal [25]. At low alkali metal coverages, an initial decrease of the work function of the transition metal surface is observed, reaching a minimum at an alkali coverage of the order of 0.25, and by an increase to a work function that approaches the bulk alkali metal work function. In the case of K/Au(111), K adsorbs in its cationic state at low coverages [26]. When approaching

high coverage ($\theta = 0.7$), K depolarizes to a metallic state and the Au(111) surface work function is lowered by 3 eV [26]. This behavior is general for all transition metal surfaces and independent of temperature for alkali adsorption temperatures below the onset of desorption of the first alkali layer [25]. Furthermore, adsorption of Na and K followed by annealing can lead to the reconstruction and formation of mixed alkali-Au surfaces [27-38]. A similar phenomenon is observed on Pd and other late transition metals [31]. The implication of electronic and morphological changes to Au surfaces (as well as impacts to Au-alloy formation) instigates further investigation for pathways of chemisorbed O_2 activation required for oxidation reactions performed by Au and bimetallic Au alloy catalysts.

There are periodic trends across the alkali metals, including in atomic radius, ionization energy, electronegativity, melting and boiling points, and density. The atomic radius is determined by the number of electron shells around the nucleus and the attraction the outermost electrons experience from the nucleus. Thus, with increasing atomic number among the alkali metals, the atomic radius increases due to the increasing number of electron shells. Likewise, the ionization energy, or the energy required to remove the most loosely attracted electron from one mol of the alkali metal, decreases with increasing atomic number. Electronegativity is a measure of the tendency of an atom to attract a bonding pair of electrons, and alkali metals are characterized by low electronegativities. With increasing atomic number, the electronegativity decreases. The melting and boiling points of alkali metals both decrease and density increases with increasing atomic number. If alkali metal electron orbitals exist roughly as spheres around a nucleus and the alkali metal sits on a catalyst metal surface or even within the alloy, the polarization of the surface caused by the forementioned chemical properties would occur in both the x and y-direction but also the z-direction allowing for different alkali metals to promote or poison a reaction by alternate mechanisms.

In the present work, a series of alkali (Li, Na, K, Cs) promoted $PdAu/SiO_2$ catalysts were prepared and tested in the gas-phase oxidative coupling of methanol and DMA to form dimethylformamide (DMF). Samples were prepared by SEA using group 1 alkali salts. Unlike NH_4OH, whose cation (NH_4^+) is removed during the reduction step (likely desorbing as NH_3), the alkali metals persist on the surface of the catalyst and support after reduction leading to alkali-doped supported nanoparticle catalysts. With this study, we aim to investigate the impact of residual alkali metals on the catalyst after SEA syntheses as promoters or poisons for oxidative coupling on $PdAu/SiO_2$ catalysts.

2. Experimental Methods

2.1 Catalyst Synthesis

Amorphous silica supports (Si-xerogel) were prepared following the procedure from van Grieken et al. [39]. A solution of 8.01 g of 0.1 M HCl (Sigma, 37%), 80 g of tetraethylorthosilicate (TEOS; Sigma, 98%), and 100 g of Millipore H_2O (18.2 MΩ) were stirred in a clean, 500 cm^3 PFA jar (Savillex) for 2 hours at 750 rpm and ambient temperature to allow for complete TEOS hydrolysis. After 2 hours, 1 M NH_4OH (Sigma) was added dropwise while stirring until the solution formed a gel. The gel was broken up with a plastic spatula until a fine powder formed, and the stir bar was removed. The gel was then dried at 433 K for 24 hours in a gravity convection oven with the cap loose on the PFA jar in order to avoid over-pressurizing the container. The recovered dry solids were ground into a fine powder using a mortar and pestle and washed six times by vortex mixing with Millipore water (18.2 MΩ; 35 cm^3 per wash vial) each time recovering the solids by centrifugation (10,000 rpm, 300 s). After six washes, the resultant supernatant had a

pH of 5.5. The washed solids were dried again at 433 K for 24 hours and then calcined in flowing air (1.67 $cm^3\ s^{-1}\ g^{-1}_{solid}$) at 823 K (0.0167 K s^{-1} ramp rate) for 10 hours.

Au bis-ethylenediamine (AuBEN) was synthesized following the procedures discussed in previous literature [13, 40]. AuBEN was made by first dissolving 0.2529 g of $HAuCl_2$ (VWR, ≥99.9%) in 2.5 cm^3 of diethyl ether (VWR, reagent grade) in a PFA jar. In a separate PFA container, 0.25 cm^3 of 1,2-ethanediamine monohydrate were mixed with 1.25 cm^3 of diethyl ether (VWR, reagent grade). The two solutions were delicately added together as the resultant reaction is exothermic and occurs quickly which is evident through observed gas evolution. The resulting solution maintained a vibrant orange color. 0.7 cm^3 of Millipore H_2O (18.2 MΩ) were added to the solution followed by 3.75 cm^3 of ethanol (VWR, ≥99.9%) to precipitate the solid. 0.7 cm^3 of Millipore H_2O (18.2 MΩ) was added to the solution again to dissolve the solid followed by 15 cm^3 of ethanol to precipitate the solid a second time. The solids were recovered by centrifugation (10,000 rpm, 600 s) with the liquid layer pipetted off and the solids dried by evaporation to the room in darkness for 72 hours in ambient conditions (room temperature and atmospheric pressure). 0.0602 g of product was recovered after this step, which was the Au-precursor, AuBEN.

All of the bimetallic $PdAu/SiO_2$ catalysts were synthesized by strong electrostatic adsorption (SEA) methods described by Dong et al. [10]. The only notable difference is the change in the salt of the base used to negatively charge the support structure. The target weight loading was 0.02 g PdAu in 1.00 g silica, and the desired Pd:Au molar ratio was 1:5. First, 100 ppm solutions of PdTAN (Tetraamminepalladium nitrate, Sigma 10 wt% in H_2O) and AuBEN were prepared by diluting 10 wt% PdTAN in H_2O (Sigma, >99.99%) with Millipore H_2O (18.2 MΩ) and by dissolving in-house synthesized AuBEN in Millipore H_2O (18.2 MΩ). The volume of precursor solution used for each synthesis was determined by the support surface area and the mass of the support (1000 $m^2\ L^{-1}$). The surface area of Si-xerogel was measured to be 400 $m^2\ g^{-1}$. Roughly 18.66 cm^3 of the 100 ppm PdTAN solution was mixed with 150 cm^3 of the 100 ppm AuBEN solution in a PFA jar, and the pH of the solution measured with Mettler Toledo FiveEasy Plus pH meter. The pH of the solution was adjusted to 10.5 pH with one of the following 4 M solutions: NH_4OH (Sigma), LiOH (Sigma, 99.95), NaOH (ThermoScientific, 97%), KOH (Sigma, >95%), and CsOH (BTC, 99.9%). Precise pH control was achieved by additions of small volumes of base solution and real-time pH measurements as to prevent overshooting the desired pH of 10.5. Next, 0.972 g of finely ground Si-Xerogel were mixed into the precursor solution. The pH was again adjusted to 10.5 by adding the same 4 M base solutions used in the previous step. The mixture was left to stir with the pH measured and adjusted periodically until the pH remained steady at 10.5 between successive measurements (typically after ~1 hour of stirring). It is worthwhile emphasizing keeping a careful eye on the pH meter as the pH will continue to decrease. The powder was reclaimed from the solution by centrifugation (10000 rpm, 300 s). After removing the water layer, the centrifuge tubes containing the wet powder product were wrapped in tin foil to create a dark environment and placed in a ventilated drying oven at room temperature at a vacuum pressure of 22.8 Torr for at least 24 hours. Once dry, the powders were reduced in a tube furnace at 673 K for 1 h under 20% H_2 in He (0.0167 K s^{-1} ramp rate, total flow of 1.67 standard $cm^{-3}\ s^{-1}\ g^{-1}_{solid}$).

2.2 Catalyst Characterization

Bulk elemental composition and total weight loading of synthesized samples were measured by inductively coupled plasma-optical emission spectroscopy (ICP-OES, Agilent 5800). Approximately 0.050 g of powder sample were digested in a 125 cm^3 polytetrafluoroethylene

(PTFE) jar with 2 cm^3 of hydrofluoric acid (48%, VWR) for 24 hours. Then, aqua regia was produced by combining 3 volume parts HCl (37%, Sigma) and 1 volume part HNO_3 (70%, Sigma). 1 cm^3 of aqua regia was added to the PTFE jar to further digest metal particles not dissolved by the HF. Following an additional 24 hours of digestion, the mixtures in the PTFE jars were diluted with 2% HNO_3. Calibration standards (1000 ppm, Sigma) for Pd, Au, and respective alkali elements were made to span the concentration ranges of 0.01-5 ppm. Immediately before testing the dissolved samples, the Agilent 5800 was calibrated with the forementioned calibration standards. Each standard and sample solution were measured three times and averaged for accuracy. The entirety of the standards and samples were measured within 2 hours of instrument uptime, and machine drift was considered to be a nonfactor. The most prominent OES peak for cesium (894.3 nm) is outside of the detection range capable of the Agilent 5800 (167-785 nm). Due to the insensitivity of less distinguishable Cs wavelengths (455.5 and 459.3 nm), elemental analysis of Cs was performed by flame atomic absorption spectrometry (FLAA) at Galbraith Laboratories, Knoxville, Tennessee by GLI Procedure ME-71.

Ex situ X-ray adsorption spectroscopy (XAS) measurements were performed at beamline 9-3 [41] using a Si(220) double crystal monochromator at the Stanford Synchrotron Radiation Lightsource (SSRL) at SLAC National Accelerator Laboratory. Spectra were collected at ambient temperatures and pressure on as-synthesized PdAu-Cs/SiO_2 and PdAu-K/SiO_2 samples at the Pd-K edge (24350 eV) to gain insight into the local structure of Pd atoms within the alloyed particles. Powders were pressed into pellets and placed on Kapton tape, which was subsequently folded to secure the pellet inside. Four scans were taken of each sample. The Demeter software suite was used to analyze all data [42]. X-ray absorption fine structure (EXAFS) data were fit to a crystallographic information file (CIF) for cubic Au metal [43], with the center Au and two neighboring Au replaced with Pd to model the alloy, as well as a Pd-O path from palladium oxide [43]. An amplitude reduction factor of 0.81 ± 0.04 was determined from EXAFS fitting of Pd foil spectra collected on this beamline and used to calculate coordination numbers for Cs and K promoted samples. EXAFS spectra were fit between 1.15-3.4 Å, between k-values of 3.2-13.1, and with k 1 and 2 fitting weights. The σ^2 for the Pd-Pd path from the fit of PdAu-K/SiO_2 was constrained to the value obtained from this path from the fit of PdAu-Cs/SiO_2. The same Pd foil data was used as a standard for linear combination fitting, along with PdO reference data obtained from Co-ACCESS.

In situ XAS measurements were performed at Inner Shell Spectroscopy beamline 8-ID [44] at the National Synchrotron Light Source II (NSLS-II) at Brookhaven National Laboratory (BNL) using a Si(111) double crystal monochromator. Unsieved PdAu-Na/SiO_2 was loaded into a 1.8 mm i.d. polyimide capillary tube (Cole-Parmer) and held in place on both ends with quartz wool pads. After taking scans at ambient temperature, the sample was heated to 398 K (0.167 K s^{-1} ramp rate) under flowing He (0.33 cm^3 s^{-1}). After taking scans at 398 K under He, the sample was then heated further to 523 K (0.167 K s^{-1} ramp rate) under 20% O_2 in He (0.33 cm^3 s^{-1} total flow) and held for 1 hour to mimic the normal pretreatment done in the kinetic reactor apparatus at UA. After 1 hour, the sample was cooled to 398 K under flowing He (0.33 cm^3 s^{-1}), and more scans were taken at 398 K. For *operando* studies, the sample was held at 398 K under reaction conditions (0.33 cm^3 s^{-1} total flow: 8.5% O_2 in He flowed through a saturator containing 0.5 mol L^{-1} DMA in methanol) while collecting spectra. Spectra were also collected under excess O_2 (0.33 cm^3 s^{-1} total flow: 40% O_2 in He), and while co-feeding water (0.33 cm^3 s^{-1} total flow: 40% O_2 in He flowed through saturator containing 0.5 mol L^{-1} DMA, 0.1 mol L^{-1} water in methanol). At least ten scans were taken each time. Within the Demeter software suite, EXAFS data was fit to the same alloy model

discussed previously, with a Pd-O path from palladium oxide [43] added to fit spectra collected under reaction conditions. An amplitude reduction factor of 0.65 ± 0.03 was obtained from EXAFS fitting of Pd foil spectra collected on this beamline and used to calculate coordination numbers for *in situ* data. EXAFS spectra were fit between 1.2-3.6 Å, between k-values of 3.3-10.8, and with k 1 and 2 fitting weights. Spectra collected at 298 K and 398 K under He before reaction were each fit modeling the σ^2 term as purely a fitting parameter, and with a Debye-Waller model, yielding similar results for Pd and Au coordination numbers (See section S.8). As a result, all other *in situ* spectra were fit modeling the σ^2 term as just a fitting parameter. The σ^2 term for the Pd-Pd path for data collected under excess oxygen was constrained to the value obtained from the fit of spectra collected after 70 min reaction under normal conditions.

The surface areas of Si-xerogel and synthesized catalysts were measured by N_2 physisorption at 77 K using a Micrometrics ASAP2020 Plus. Glass vacuum sample tubes were cleaned with Millipore H_2O (18.2 MΩ) and acetone (≥99.5% VWR) and left to dry in an oven at 363 K for 24 hours. Then, ~0.050 g of powder sample was pelleted and sieved to 180-250 μm and loaded into the glass vacuum sample tube. The samples were first degassed by pulling vacuum (~1 μmHg) and heating the sample to 623 K (0.167 K s^{-1}) and held for 9 hours. To access the mass of moisture lost during degassing, the glass vacuum tube and sample were reweighed and compared to the mass of the sample tube and sample prior to degassing. The degassed sample mass was used for analysis for accuracy. The glass vacuum sample tube containing the sample was placed into the analysis port of the ASAP2020 Plus for collection of the N_2 isotherm at 77 K.

High resolution transmission electron microscopy (HRTEM) images were collected on a Thermo Fisher Talos 200i. Bright-field and dark-field images were collected at 200 kV. Dark-field images were collected using the HAADF detector, a condenser 2 (C2) aperture of 50, and a spot size of 4. Images were collected at a resolution of 2048×2048 at a dwell time of 20 μs. EDS scans were collected with a C2 aperture of 100, a spot size of 3, and a camera length of 98 mm. Scans were run at a dwell time of 16 μs in a resolution of 1024×1024. Typically, a full EDS map scan time was 720 s. Within the Velox analysis software, pre-filtering was used with an averaging the net% of 3 pixels. Surface-weighted average particle diameters, dispersion, and dispersity index (DI) were determined by collected TEM images by the methods previously reported [6, 45, 46].

XRD patterns were collected using a Rigaku SmartLab with a Cu kα X-ray source at 40 kV and 44 mA. Finely ground sample powders were loaded into a Rigaku zero background holder and leveled with a glass slide in a small circular motion. Scans ranged from 10° to 50° 2θ at increments of 0.05° and a scan rate of 0.0167° s^{-1}.

DRIFTS spectra were collected with Vertex V-70 FTIR equipped with a mercury-cadmium-telluride detector, and Bruker OPUS 6.2 software was used to analyze the spectra. Finely ground sample powder was loaded into a Harrick Praying Mantis high temperature reaction chamber with KBr windows (HVC-DRP-5) and leveled with the top of the cup using a flat plastic spatula. The reaction chamber was mounted into the Harrick Praying Mantis Diffuse Reflectance Accessory. Pure N_2 was passed through the chamber at 0.33 cm^3 s^{-1} while the chamber was heated from 308 K to 578 K at 0.167 K s^{-1} to dehydrate the sample powders. The reaction chamber was cooled back to 308 K at 0.167 K s^{-1} before Kubelka-Munk spectra was collected between 4000 cm^{-1} to 400 cm^{-1} at a resolution of 2 for 200 scans. Pure KBr powder under N_2 flow was given the same temperature treatment and was used to collect a background applied to all sample spectra.

O_2 temperature programmed desorption (TPD) experiments were conducted with a Micromeritics Autochem II 2920 equipped with a thermal conductivity detector (TCD). Sample powders were pelleted and sieved to 180-250 μm, approximately 0.1 g of sieved powder was

loaded into the U-tube quartz reactor and held in place with quartz wool. First, a pretreatment similar to the procedure performed the flow reactor (discussed in section 2.3) was employed to remove moisture and draw Pd to the catalyst surface [47]. The powders in the U-tube reactors were heated in 20% O_2 and He at 0.83 $cm^3\ s^{-1}$ to 523 K (0.083 K s^{-1}), held for one hour, and then cooled back to ambient temperature. Next, the catalyst bed was saturated with pure O_2 by flowing 0.83 $cm^3\ s^{-1}$ at ambient temperature for one hour before purging with 0.83 $cm^3\ s^{-1}$ He for 1800 s. Then, the flow rate of He was increased to 1.67 $cm^3\ s^{-1}$ and the temperature was increased from ambient temperature to 673 K at 0.5 K s^{-1} while the effluent gas was monitored with the TCD. Before experimenting, the TCD was calibrated with O_2 using He as a reference gas.

2.3. Kinetic Studies

Kinetic studies were conducted using a continuous flow packed bed reactor. A process flow diagram of the system can be found in the supporting information (Figure S.1). The samples of the effluent stream were analyzed utilizing an Agilent 6890N/5975 GC/MS with a switching valve and sample loop system. The 6890N was equipped with an Alltech AT-Q (30 m × 0.53 mm) and Restek Shincarbon ST (2 m × 1 mm) in series to separate permanent gases for analysis with a TCD. An Agilent Porabond U column (25 m × 0.32 mm × 7 μm), used for hydrocarbon separation, which fed into a splitter that split the separated stream to an FID and the 5975 MS.

The packed catalyst bed typically consisted of 15 mg or less of sieved catalyst grains (180 -250 μm) diluted with an additional quantity of sieved Si-xerogel to create a catalyst bed between 30 mg and 40 mg and a bed length of 3 mm. The volumetric flow rate through the reactor was ~1.67 $cm^3\ s^{-1}$. This high space velocity and low catalyst loading ensured differential conversion of reactants (less than 10%). Upon loading fresh catalyst, the catalyst was pretreated using mild oxidation procedures from Luneau et al. [48]. The pretreatment procedure was 0.83 $cm^3\ s^{-1}$ of synthetic air (20 kPa O_2 and 30 kPa N_2) while ramping the reactor bed temperature from 298 K to 523 K at 0.033 K s^{-1} and holding at 523 K for 3600 s. The reactor bed was cooled to 398 K before reactants were passed to the catalyst bed. The standard condition used was 398 K, 120 kPa total pressure, 2.4 kPa methanol, 1.2 kPa O_2, 0.08 kPa DMA, 1.2 kPa CH_4 (internal standard), and a balance He. Following a kinetic measurement, the catalyst bed was kept at 398 K under flowing inert gas (typically 0.83 $cm^3\ s^{-1}$ of Ar), while the reactant stream was diverted to bypass the catalyst bed. At least four GCMS injections were taken and averaged to determine reactant concentrations and calculate conversion.

When investigating reaction orders and activation energies, experiments began and ended at this standard condition which allowed for exponential deactivation to be fitted and applied to the data. The exponential deactivation trend (e^{kt}) for each product species, *i*, and each product species rate at the first standard condition ($r_{i,o}$) were used in equation 1 to correct data and obtain a corrected rate ($r_{corrected}$).

$$r_{corrected} = \frac{r_{i,o}}{e^{kt}} \qquad \text{(eq. 1)}$$

Conversion, *X*, was calculated with molar flowrate, *f*, of each reactant, *i*, measured in reactor bypass, *b*, and molar flowrate each of reactant in the effluent stream, *s*, from the catalyst bed (equation 2).

$$X_i = \frac{f_{i,b} - f_{i,s}}{f_{i,b}} \qquad \text{(eq. 2)}$$

All selectivity data is reported as carbon selectivity. To calculate carbon selectivity, S_i, the number of carbons in each product species, *i*, was divided by the total number of carbons, *n*, in

carbon-containing reactants on a molar flowrate basis, *f*. An index *a* is used for all reactants in equation 3.

$$S_i = \frac{n_i * f_i}{\Sigma(n_a * f_a)} \quad \text{(eq. 3)}$$

3. Results and Discussion

3.1 Catalyst Characterization

Surface area measurements were performed on each 1:5 $PdAu/SiO_2$ and are reported together in Table 1. Surface areas of the powders ranged from 200 - 400 $m^2\ g^{-1}$. A decrease in surface area of the xerogel was measured when nanoparticles are introduced to the surface. Another decrease of surface area is observed when alkali salts were used during synthesis, this decrease was more pronounced with the larger alkalis (K and Cs) than it was for Li. In addition to a reduction of measured surface area, the t-plot method [49] indicated a reduction of micropore volume of the silica. Surface areas (Table 1) and micropore volumes are summarized together in Table S.1. Plots of offset (350 $cm^3\ g^{-1}$ STP offset) N_2 isotherms are plotted in Figure S.2. and S.3 shows the micropore region with no offset applied to the isotherms to allow for graphical comparison of micropore volume. The reduction in surface area and micropore volume of the Si-Xerogel are likely from pore filling of nanoparticles and alkali metals post-synthesis.

Results of Pd:Au ratio and overall transition metal weight loading measured by ICP-OES and FLAA are described in Table 1. Generally, Pd:Au ratios deviate by no more than ± 1 Pd molar equivalents per 5 moles of Au from the target molar ratio of 1:5 Pd:Au. Significant differences were measured in alkali content between the promoted samples and no ICP data was collected for Cs as the most prominent ICP peak for Cs occurs at 894 nm which is above the detection range for the Agilent 5800. Attempts to monitor the 455 nm and 459 nm peaks for Cs were made but no distinguishable peak could be detected at the levels of Cs present. Despite similar molar quantities of alkali bases used in the synthesis of each sample, molar uptake of alkali metal per gram of catalyst varied. Li uptake was measured at $3.5 \cdot 10^{-4}$ mol g^{-1}, uptake of Na was $1.8 \cdot 10^{-4}$, and K uptake was $6.8 \cdot 10^{-4}$ mol g^{-1}. FLAA analysis performed by Galbraith Laboratories (GLI Procedure ME-71) reported a Cs loading of $6.8 \cdot 10^{-4}$ mol g^{-1}, similar to the K sample. It is unclear whether these variations in uptake are due to differences in uptake chemistry during synthesis, and analysis of such principles is beyond the scope of this study.

Synthesis of alkali promoted 1:5 $PdAu/SiO_2$ yield particles with surface-weighted average particles diameter typically around 5 nm (Figure 1, Table 1). Size and dispersion of metal nanoparticles have been reported to be influenced by the presence of alkali metals [17, 50-54]. However, electron microscopy reveals no significant pattern to particle size or dispersion related to the introduction of alkali metals during synthesis. While surface weighted particle diameters vary among samples, standard deviations overlap and suggest that particle sizes of bulk samples are similar. TEM images and the size distribution graph of unpromoted 1:5 $PdAu/SiO_2$ can be found in supporting information (Section S.3, Figure S.4).

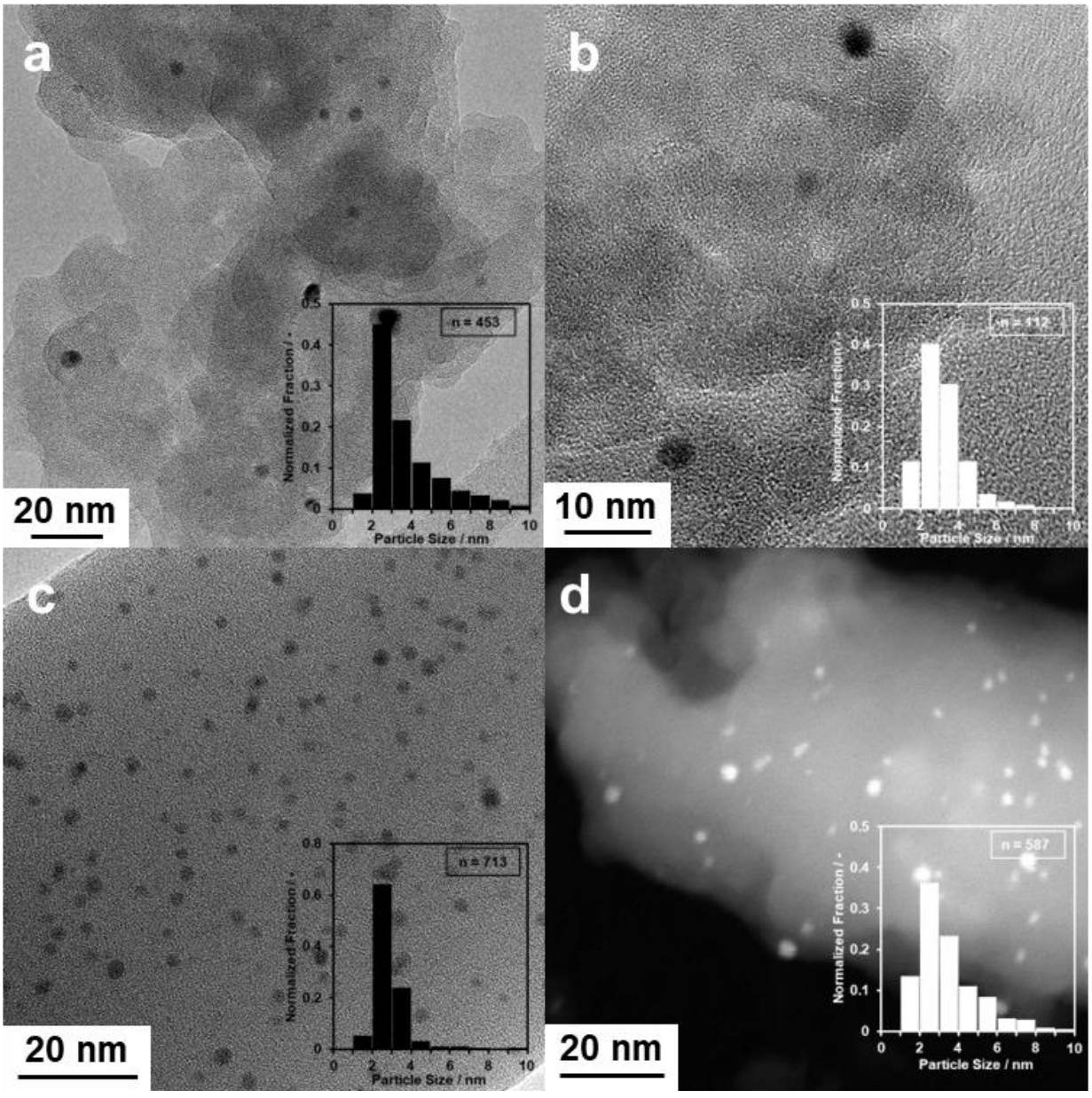

Figure 1. TEM images and inset particle size distributions for (a) 1:5 PdAu-Li/SiO_2, (b) 1:5 PdAu-Na/SiO_2, (c) 1:5 PdAu-K/SiO_2, (d) 1:5 PdAu-Cs/SiO_2.

Table 1. Results of the Physical Characterization of $PdAu/SiO_2$ Catalysts.

Sample	Total Pd+Au Loading / mol g^{-1} [a]	Alkali Metal Loading / mol g^{-1} [a]	Molar Pd:Au Ratio [a]	S_{BET} / m^2 g^{-1} [b]	As Prepared Surface-weighted average particle diameter / nm [c]	Used Surface-weighted average particle diameter / nm [c]	Dispersion	Dispersity Index [d]
$PdAu/SiO_2$	$3.6•10^{-5}$	-	1:5	340 ± 6	5.4 ± 1.6	6.1 ± 1.7	0.19	1.2
PdAu-Li/SiO_2	$3.6•10^{-5}$	$3.5•10^{-4}$	1:6	300 ± 5	6.1 ± 1.9	-	0.19	1.6
PdAu-Na/SiO_2	$4.3•10^{-5}$	$1.8•10^{-4}$	1:6	250 ± 4	3.9 ± 1.1	-	0.29	1.2
PdAu-K/SiO_2	$4.6•10^{-5}$	$6.8•10^{-4}$	1:5	200 ± 3	4.3 ± 1.1	-	0.27	1.5
PdAu-Cs/SiO_2	$3.6•10^{-5}$	$6.8•10^{-4}$ [e]	1:6	220 ± 3	5.5 ± 1.7	4.1 ± 1.0	0.28	1.2

[a] Bulk elemental composition and weight loading determined by ICP-OES.
[b] Surface Area measurements determined by N_2 physisorption performed at 77 K.
[c] Surface-weighted average particle diameter measured by TEM.
[d] Dispersity index calculated from TEM images where DI <1.5 is considered monodisperse [46].
[e] Measured by FLAA analysis.

Ex situ X-ray absorption spectroscopy data is shown in Figure 2 for both PdAu-Cs/SiO_2 and PdAu-K/SiO_2. XANES spectra suggest that most of the Pd in Cs and K promoted samples are in the metallic state, but some may also be oxidized. Linear combination fitting (LCF) in Athena using metallic Pd and PdO as standards suggests that PdAu-K/SiO_2 is 83% metallic and 17% oxide, while PdAu-Cs/SiO_2 is 91% metallic and 9% oxide. LCF plots can be found in Section S.4. The results of fitting Fourier-transform EXAFS spectra are summarized in Table 2**.** Plots of these fits in both k and R space can be found in Section S.4. The Pd in these samples was mostly coordinated to Au, with smaller contributions from Pd and O. This suggests that the samples are alloyed, but there may be some local Pd aggregation, and aggregates near the surface may become partially oxidized [55]. The total Pd coordination number being closer to 9 than to 12 also suggests that these nanoparticles have significant amounts of surface Pd [55]. These results are in agreement with the linear combination fit that PdAu-K/SiO_2 is more oxidized than PdAu-Cs/SiO_2, as the EXAFS fit of PdAu-Cs/SiO_2 had a higher Pd-Au coordination number, and the LCF predicted this sample was more metallic compared to the K-promoted sample.

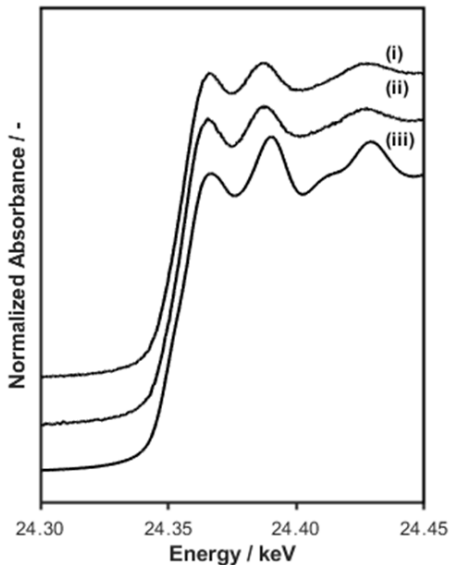

Figure 2. Ex situ Pd K edge XANES of (i) PdAu-K/SiO_2, (ii) PdAu-Cs/SiO_2, (iii) Pd foil.

Table 2. Radial bond distances, coordination numbers, mean squared disorder, change in absorption edge energy, and R factor obtained from EXAFS fitting.

Sample	Path	d / Å	CN	σ^2 / Å^2	ΔE_0 / eV
PdAu-Cs/SiO_2	Pd-Au	2.81 ± 0.01	9.9 ± 1.9	0.0086 ± 0.0017	0.7 ± 1.5
	Pd-Pd	2.79 ± 0.06	0.2 ± 0.4	0.0007 ± 0.0095	0.7 ± 1.5
	Pd-O	1.98 ± 0.07	0.4 ± 0.4	0.0002 ± 0.0081	-2.1 ± 14.7
PdAu-K/SiO_2	Pd-Au	2.80 ± 0.01	8.7 ± 1.7	0.0095 ± 0.0019	0.8 ± 1.3
	Pd-Pd	2.77 ± 0.08	0.1 ± 0.1	0.0007	0.8 ± 1.3
	Pd-O	1.99 ± 0.04	0.6 ± 0.3	0.0002 ± 0.0041	4.0 ± 7.1

In situ XANES measurements were performed over the Na-promoted sample (Figure 3), and given the minimal changes upon variations in reaction conditions, only *ex situ* experiments were performed for the Cs- and K-promoted samples (Figure 2). These spectra suggest that the Pd remains in the metallic state during reaction, even under a large excess of oxygen. The results of fitting Fourier-transform EXAFS spectra are summarized in Table 3. Plots of these fits in both k and R space can be found in Section S.4. Attempting to add a Pd-O path to fit models before starting the reaction and under 8.5% O_2 resulted in a negative coordination number for the Pd-Pd path. The Pd in this sample is mostly coordinated to Au, suggesting that the sample is alloyed, in agreement with the XANES. Similarly to the *ex situ* XAS data, the total coordination number was closer to 9 than to 12, suggesting surface-alloying rather than bulk-alloying [55]. When the oxygen mol fraction in the feed was increased from 8.5% to 40%, the Pd became partially oxidized, and remained oxidized even when water was co-fed, in agreement with XANES data showing these spectra had a higher E_0 than before the reaction and than when the oxygen mole fraction in the feed was 8.5%. There is also a corresponding decrease in the Pd-Au coordination. Since no oxidation was observed after 4.2 ks under 8.5% O_2, we assume that the Pd in these samples would remain metallic at the standard 1% O_2 used for catalytic testing. Additional plots of XAS data and fitting models are reported in Section S.4 of the Supporting Information.

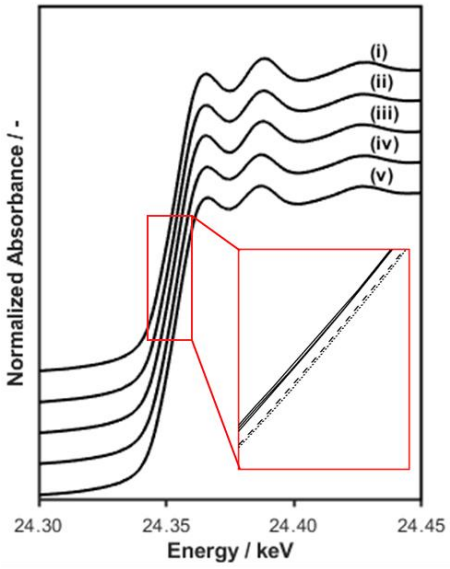

Figure 3. *In situ* Pd K edge XANES of PdAu-Na/SiO_2 offset vertically for ease of comparison (i) under He at 298 K before reaction, (ii) under He at 398 K after pretreatment, (iii) after 4200 seconds under normal reaction conditions, (iv) under excess oxygen, (v) under excess oxygen with water co-feed. Insert: spectra plotted without vertical offset to show shift in white line intensity from left to right. Under excess oxygen (dashed), under excess oxygen with water co-feed (dotted), all others solid.

Table 3. Radial bond distances, coordination numbers, mean squared disorder, change in absorption edge energy, and R factor obtained from EXAFS fitting during *in situ* experiments with PdAu-Na/SiO_2.

Condition	**Path**	**d / Å**	**CN**	**σ^2 / Å^2**	**ΔE_0 / eV**
298 K under He	Pd-Au	2.78 ± 0.01	9.61 ± 0.77	0.0091 ± 0.0011	-0.57 ± 0.49
	Pd-Pd	2.75 ± 0.02	0.37 ± 0.20	0.0022 ± 0.0039	-0.57 ± 0.49
398 K under He post pretreatment	Pd-Au	2.79 ± 0.01	10.2 ± 1.0	0.0126 ± 0.0015	-0.52 ± 0.60
	Pd-Pd	2.79 ± 0.03	0.22 ± 0.20	0.0007 ± 0.0054	-0.52 ± 0.60
398 K after 4.2 ks reaction	Pd-Au	2.79 ± 0.01	9.55 ± 0.85	0.0107 ± 0.0012	-1.14 ± 0.52
	Pd-Pd	2.74 ± 0.03	0.24 ± 0.19	0.0017 ± 0.0048	-1.14 ± 0.52
398 K under excess O_2	Pd-Au	2.81 ± 0.03	7.58 ± 3.26	0.0099 ± 0.0049	0.27 ± 1.99
	Pd-Pd	2.80 ± 0.06	0.37 ± 0.35	0.0017	0.27 ± 1.99
	Pd-O	2.01 ± 0.16	0.49 ± 0.77	0.0070 ± 0.0208	1.36 ± 24.37
398 K under excess O_2 water co-feed	Pd-Au	2.81 ± 0.02	7.14 ± 2.64	0.0093 ± 0.0041	0.26 ± 1.99
	Pd-Pd	2.79 ± 0.06	0.37 ± 0.32	0.0017	0.26 ± 1.99
	Pd-O	2.01 ± 0.13	0.52 ± 0.69	0.0069 ± 0.0175	2.33 ± 18.78

DRIFTS spectra (Figure 4) collected for powder samples prepared with alkali hydroxides during SEA showed decreasing intensity in the OH-stretching region (range 3000-4000 cm^{-1}) assigned to silanol groups at the surface of amorphous silica [56]. As previously shown by Díaz et al. [57], the intensity of the silanol O-H peak decreases when the alkali ions are present on silica. In comparison, the spectra of the Si-xerogel support and the unpromoted $PdAu/SiO_2$ catalyst were identical, with much greater total band area than the alkali-containing samples (Figure 4). Subtracted spectra (for each sample spectra with Si-xerogel support subtracted) are provided in Figure S.18. A negative band at 3750 cm^{-1} was observed for each of the alkali-containing samples suggesting removal of surface silanol groups. During synthesis and drying procedures, it is presumed that alkali ions in solution cap a portion of the surface silanol groups and form small domains of alkali silicates, while the bulk remains SiO_2. PdAu nanoparticles sitting on or in the proximity of the surface alkali silicates may be influenced by the presence of the electropositive alkali metals. It is expected that the formation of orthosilicates or disilicates is improbable given the amorphous nature of the Si-xerogel. X-ray diffraction patterns (Figure S.19) for all samples had no distinguishable peaks other than the broad peak assigned to amorphous silica at 20°. Consistent with the DRIFTS spectra, if small domains of alkali silicates were created at the surface, these were undetectable by XRD, and the bulk of the silica remains amorphous SiO_2. The lack of peaks for Au(111) or Pd(111) (38° and 40°, respectively) confirms a majority of the PdAu nanoparticles on the support are small and disperse.

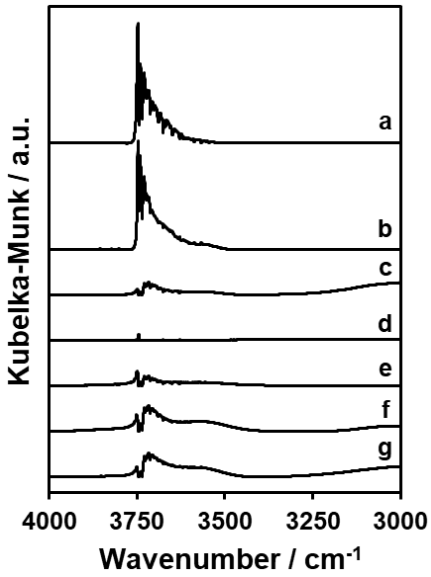

Figure 4. DRIFTS spectra in the O-H stretching region. (a) Si-xerogel (b) 1:5 $PdAu/SiO_2$ (c) K/SiO_2 (d) 1:5 PdAu-Li/SiO_2 (e) 1:5 PdAu-Na/SiO_2 (f) 1:5 PdAu-K/SiO_2 (g) 1:5 PdAu-Cs/SiO_2.

O_2-TPD profiles (Figure 5) showed that almost no O_2 was chemisorbed to the alkali-free 1:5 $PdAu/SiO_2$ catalyst. Samples with Na, K, and Cs exhibit a desorption peak with a maximum at similar temperature (382-386 K) but varied total O_2 desorbed. The desorption peak maxima for Na, K, and Cs doped samples occurred at 385 K, 382 K and 386 K, respectively. More O_2 desorbed from the Cs sample than the Na sample, but the K sample chemisorbed the most O_2. The 1:5 PdAu-Li/SiO_2 sample had a quantity of O_2 desorbed similar to the Cs sample, but the desorption peak maximum occurred at a higher temperature (421 K). Offset TPD profiles are presented in Figure S.20. Due to the differences in alkali uptake (determined by elemental analysis), moles of O_2 desorbed from the catalyst during O_2-TPD were normalized by moles of alkali. Upon this

normalization, K retains its status as the most active promoters among alkali metals tested (Figure S.21). Normalization of mols of O_2 desorbed by mol of Pd (Figure S.23) results in values all greater than unity, suggesting that O_2 chemisorption occurred at more locations on the catalyst than just exposed Pd surface sites. Ren et al. [38] reported K promotion of O_2 chemisorption on Au(111) occurs through the formation of a K_2O_2 species, but it is unclear if this structure is unique to K; the reason K specifically is most effective in assisting O_2 chemisorption is also unclear.

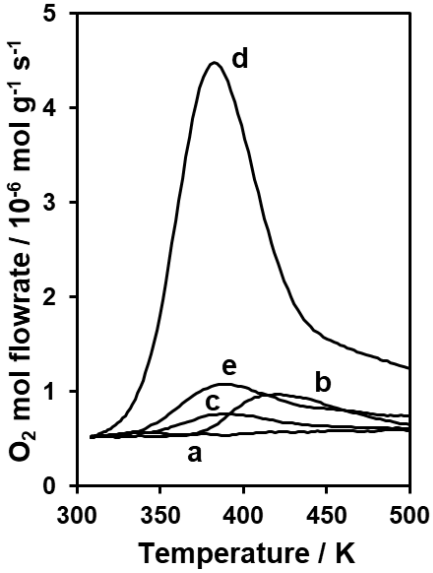

Figure 5. O_2-TPD profiles of (a) 1:5 PdAu/SiO_2 (b) 1:5 PdAu-Li/SiO_2 (c) 1:5 PdAu-Na/SiO_2 (d) 1:5 PdAu-K/SiO_2 (e) 1:5 PdAu-Cs/SiO_2.

3.2 Catalyst Performance in Oxidative Coupling

Introduction of alkali metals onto 1:5 PdAu/SiO_2 catalysts modifies several kinetic aspects of the oxidative coupling of methanol and dimethylamine (DMA) reaction. The 1:5 PdAu/SiO_2 catalyst synthesized in absence of alkali metals (NH_4OH was used as the base for pH adjustment) had a rate of dimethylformamide (DMF) formation of $2.0 \cdot 10^{-3}$ mol mol_{metal}^{-1} s^{-1} at the standard condition (Figure 6a). At these reaction conditions, DMF carbon selectivity was 95% with the remaining 5% as CO_2 (Figure 7), consistent with our prior studies of PdAu/SiO_2 catalysts prepared by SEA [6]. CO_2 likely forms from the total oxidation of methanol. No total oxidation products from DMA (e.g., NO_x species) were detected under any reaction conditions in this study, i.e., the selectivity based on nitrogen was always 100%. However, when LiOH was used for pH control during SEA (1:5 PdAu-Li/SiO_2), an additional C-N bond formation reaction occurred resulting in formation of tetramethylurea (TMU) at a rate of $0.5 \cdot 10^{-3}$ mol s^{-1} mol_{metal}^{-1} (Figure 6b) and a carbon selectivity of ~29%. This appears to be at the expense of DMF formation, as the DMF carbon selectivity decreased to 66% while the CO_2 carbon selectivity remained ~5%. With the addition of Li, the rate of DMF formation was slightly decreased (to $1.9 \cdot 10^{-3}$ mol s^{-1} mol_{metal}^{-1}, Figure 6a). However, with the rate of TMU formation included in the sum of the rates of all coupling reactions, the coupling rate was $2.4 \cdot 10^{-3}$ mol s^{-1} mol_{metal}^{-1}, higher than the alkali-free catalyst (Figure 6d). The Li promoter did result in a rate increase in CO_2 formation (from $2.1 \cdot 10^{-4}$ mol s^{-1} mol_{metal}^{-1} to $4.9 \cdot 10^{-4}$ mol s^{-1} mol_{metal}^{-1}) but the carbon selectivity for CO_2 remained 5% (Figure 7).

The 1:5 PdAu/SiO_2 catalyst synthesized in the presence of NaOH (1:5 PdAu-Na/SiO_2) resulted in an increase in the DMF production rate to $4.1 \cdot 10^{-3}$ mol s^{-1} mol_{metal}^{-1} (Figure 6a). TMU

was also produced as a product with the Na-promoted sample, and the formation rate was increased compared to the Li-promoted sample to $0.7 \cdot 10^{-3}$ mol s^{-1} mol_{metal}^{-1} (Figure 6b). With Na present on the PdAu catalyst, the methanol self-coupling product methyl formate (MF) was also observed with a formation rate of $0.9 \cdot 10^{-3}$ mol s^{-1} mol_{metal}^{-1} (Figure 6c) and a MF carbon selectivity of ~10% (Figure 7). Therefore, the carbon selectivity distribution over 1:5 PdAu-Na/SiO_2 was 68% DMF, 18% TMU, 10% MF, and 4% CO_2 (Figure 7). Notably, conversion of DMA was differential (<2%) during the collection of this data. Thus, observation of MF was not the result of complete conversion of DMA in the catalyst bed, but likely a result of the Na present on the catalyst allowing for additional coupling chemistries to occur. The overall coupling rate over the Na-promoted catalyst was greater than that measured over the Li-promoted catalyst ($5.7 \cdot 10^{-3}$ mol s^{-1} mol_{metal}^{-1}, Figure 6d), an increase in coupling rate of 2.8× relative to the alkali-free catalyst.

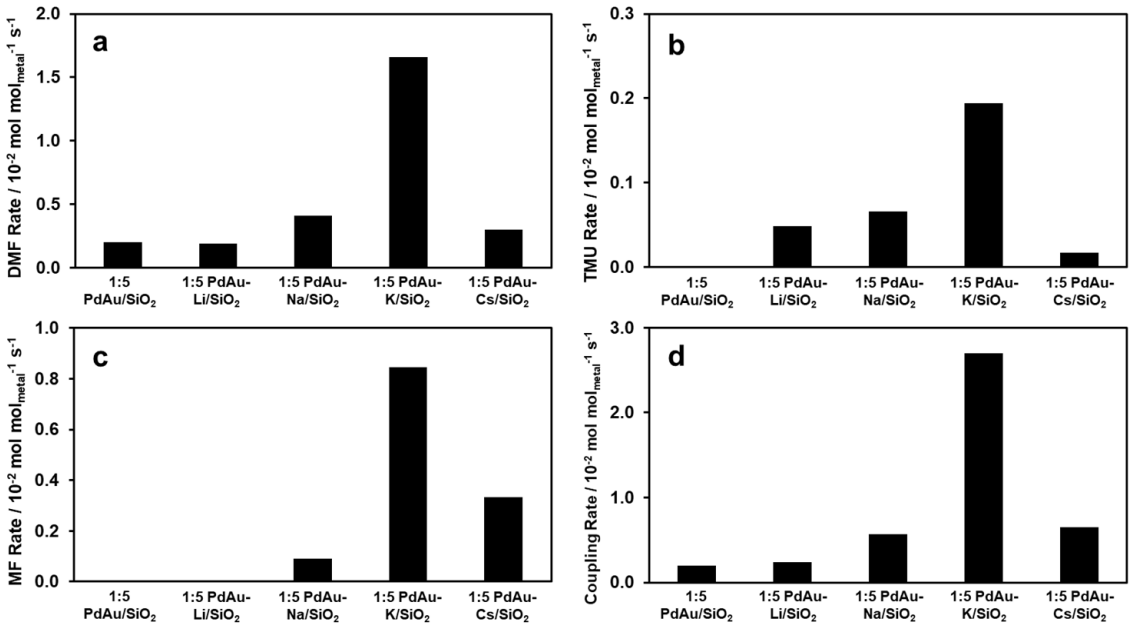

Figure 6. Comparisons of production rate of (a) dimethylformamide (DMF), (b) tetramethylurea (TMU), (c) methyl formate (MF), (d) molar sum of DMF, TMU, and MF rates. Reaction conditions: 398 K, 120 kPa total pressure, 2.4 kPa methanol, 1.2 kPa O_2, 0.08 kPa DMA, 1.2 kPa CH_4 (internal standard), balance He, 0.0043-0.0214 g of catalyst powders diluted in silica to give a consistent GHSV of 40000 hr^{-1}. Catalyst and silica diluent sieved to 180 – 250 μm.

The PdAu catalyst promoted by K (1:5 PdAu-K/SiO_2) had the highest overall coupling product formation rate of $2.7 \cdot 10^{-2}$ mol s^{-1} mol_{metal}^{-1}, a 12.5× increase compared to the unpromoted sample (Figure 6d). TMU and MF were both observed as coupling products over 1:5 PdAu-K/SiO_2. The K-promoted catalyst produced DMF, TMU, MF, and CO_2 with rates of $1.6 \cdot 10^{-2}$, $1.9 \cdot 10^{-3}$, $8.5 \cdot 10^{-3}$, and $1.7 \cdot 10^{-3}$ mol s^{-1} mol_{metal}^{-1} respectively (Figures 6a-c). Carbon selectivities were measured to be slightly different than those observed over the Na- and Li-containing samples. The carbon selectivity distribution over 1:5 PdAu-K/SiO_2 was 64% DMF, 13% TMU, 21% MF, and 2% CO_2 (Figure 7). However, the trend of increasing coupling product formation rates with increasing atomic number among the alkali metals did not hold when CsOH was used during SEA synthesis (1:5 PdAu-Cs/SiO_2), as the overall coupling product rate decreased (relative to 1:5 PdAu-K/SiO_2) in the presence of Cs to $6.5 \cdot 10^{-3}$ mol s^{-1} mol_{metal}^{-1} (Figure 6d). This overall coupling rate was 3.3× higher that the unpromoted sample. Individual product rates were $3.0 \cdot 10^{-3}$ (DMF), $0.8 \cdot 10^{-3}$ (TMU), $3.3 \cdot 10^{-3}$ (MF), and $1.8 \cdot 10^{-4}$ (CO_2) mol s^{-1} mol_{metal}^{-1} (Figure 6a-c). Carbon selectivity was distributed as 65% DMF, 15% TMU, 15% MF, and 5% CO_2 for 1:5 PdAu-Cs/SiO_2 (Figure 7). A PdAu-free K/SiO_2 sample was synthesized by SEA in absence of Pd and Au complexes to yield a powder with potassium only. K/SiO_2 was inactive at the standard test condition showing that the observed changes in rate and selectivity are due to interactions between metal nanoparticles and alkali metals and not chemistry occurring over alkali metals on silica.

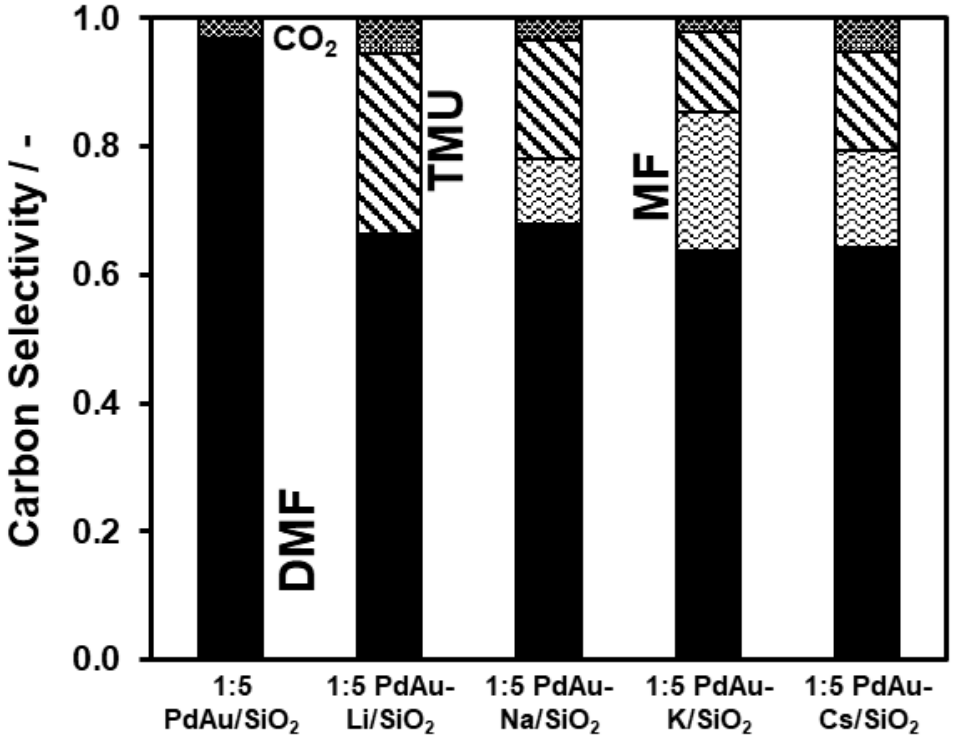

Figure 7. Carbon selectivity comparison between 1:5 PdAu/SiO_2 catalysts promoted by different alkali metals; TMF = tetramethylurea, MF = methyl formate, and DMF = dimethylformamide. Reaction conditions: 398 K, 120 kPa total pressure, 2.4 kPa methanol, 1.2 kPa O_2, 0.08 kPa DMA, 1.2 kPa CH_4 (internal standard), balance He, 0.0043-0.0214 g of catalyst powders diluted in silica to give a consistent GHSV of 40000 hr^{-1}. Catalyst and silica diluent sieved to 180 – 250 μm.

The product formation rate was plotted against trends physical descriptors (e.g., electronegativity, atomic radius, etc.) of group 1 alkali metals. While this data does not result in any discernible trends, the graphs (Figure S.31) are shown in Section S.11 of the Supporting Information. However, the coupling rate is inversely correlated with the hydrated ion radius [58, 59]. K^+ has the smallest hydrated radius [58, 59] and the greatest promotional effect. Conversely, Li^+ has the largest hydrated radius, and the smallest promotional effect (Figure 8). Plots of hydrated ion radius versus individual coupling products (DMF, TMU, and MF), versus CO_2 formation rate, and coupling rate normalized by alkali content are provided in Section S.11 (Figure S.32 & S.33).

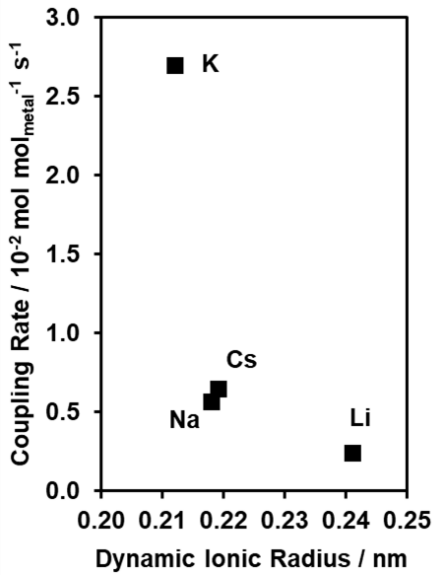

Figure 8. Coupling rate as a function of the dynamic ionic radius of hydrated alkali ions. Reaction conditions: 398 K, 120 kPa total pressure, 2.4 kPa methanol, 1.2 kPa O_2, 0.08 kPa DMA, 1.2 kPa CH_4 (internal standard), balance He, 0.0043-0.0214 g of catalyst powders diluted in silica to give a consistent GHSV of 40000 hr^{-1}. Catalyst and silica diluent sieved to

We take the observation of TMU and MF over alkali-promoted PdAu catalysts as indirect evidence that the alkali metal atoms are present on the surface of the PdAu nanoparticles, or in proximity of the nanoparticle-support interface. While methanol self-coupling has been studied with similar PdAu catalysts [1, 2, 4, 60, 61], there are no studies documenting the formation of TMU via oxidative coupling reactions (to our knowledge). The lack of comparable studies means the mechanism of the additional C-N bond formation can only be speculated upon here (Scheme S.2). We speculate that the formation of TMU occurs through a unique transition state from that for DMF formation (*vide infra*, Section 3.4). It is possible that the addition of the second surface dimethylamine occurs prior to desorption of DMF. This supposition comes from the observation that co-feeding DMF over the Cs-promoted catalyst did not increase the quantity of TMU produced (Figure S.44). Therefore, it is unlikely that TMU is a product of a second C-N bond formation to a previously formed DMF molecule that adsorbs to the surface and further reacts. While we offer a proposed mechanism for TMU formation (Scheme S.2) based on previous oxidative C-N bond formation studies [62, 63], probing the mechanism further to elucidate the pathway for TMU formation is beyond the scope of the presented study. Within Scheme S.2, the coupling reaction proceeds similar to the mechanism for DMF formation (Scheme S.1). In the abbreviated scheme, a second adsorbed DMA molecule forms a second C-N bond with the carbonyl carbon of an

absorbed DMF molecule. An additional H-removal step is required to form TMU, resulting in the carbon atom that originated from methanol without any C-H bonds.

3.3 Role of the Promoter

The role of the alkali promoter in this system is theorized to assist in oxidation of the PdAu surface. This mode of promotion may come from alkalis on the silica support near the PdAu interface as well as alkali metals directly in contact with the nanoparticles [7, 64, 65]. Alkali ions are adsorbed on the surface of the silica during SEA, when basic conditions deprotonate surface silanol groups [10, 14, 15, 66]. A $Si\text{-}O^{-}\text{-}A^{+}$ species (where A^{+} designates an alkali cation) likely forms, and potentially serves as a stronger anchoring site for formation of metal particles than silanol groups, as observed previously in K^{+}-promoted Pt@silicalite-1 [67] and Pd@silicalite-1 [68] catalysts. While no observable change in particle size was detected by imaging for the $PdAu/SiO_2$ catalysts synthesized, the uniform distribution of alkali metals over the silica support detected in EDS (Figure S.5), and the decrease in the band area for O-H stretching was observed in DRIFTS (Figure 4) suggests a similar phenomenon is occurring at terminal silanol groups of the Si-xerogel support [57, 67, 69]. We speculate that alkali metals at the metal-support interface share electrons with nearby metal atoms (in the metal nanoparticles) due to their electropositivity and low work function [22-24]. At these interfacial sites the binding of methanol may be facilitated and its partial oxidation enhanced as demonstrated in Rodiguez et al. [70] where K facilitated CO oxidation on Au/TiO_2. The increased electron density slightly lowers the work function of these perimeter atoms and other atoms nearby and increases their basicity [25]. Since the surface weighted particle diameter was invariant upon the introduction of the various alkali metals, the results of these modifications are uniquely measurements of the influence of the alkali metals in the oxidative coupling reaction. While the present study provides no direct evidence of alkali metals in physical contact with the PdAu surface or within the alloy lattice, we cannot rule out that possibility. Alkali metals at high coverages have been reported to restructure fcc lattices [27], with Na and K appearing to have to greatest impact [29, 30, 35, 71]. Au surfaces are roughened by Na and K [29, 30, 35, 71] , which could lead to unique active sites that are not present on alkali-free PdAu surfaces and allow for accelerated DMF formation in tandem with MF and TMU formation. Additionally, the uptake of alkali metal varied among the samples; when oxidative coupling rates are normalized per mol of alkali, the rate per mol alkali is greater for 1:5 $PdAu\text{-}Na/SiO_2$ than it is for 1:5 $PdAu\text{-}Cs/SiO_2$ ($1.1 \cdot 10^{-3}$ and $0.34 \cdot 10^{-3}$, respectively). Regardless of normalization, the coupling rate over 1:5 $PdAu\text{-}K/SiO_2$ was always greater than that for the other samples (e.g., $1.6 \cdot 10^{-3}$ mol (mol K)$^{-1}$ s^{-1}; Figures S.34-S.37).

3.4 Kinetic Studies of Cs Promoted 1:5 $PdAu/SiO_2$.

Next, we measured the apparent kinetics of oxidative coupling over 1:5 $PdAu\text{-}Cs/SiO_2$ in order to compare to our previous studies of $PdAu/SiO_2$ catalysts of varied particle sizes [6]. The time on stream activity was monitored to determine changes to rate and selectivity over extended use of the catalyst. Some example time-on-stream data is plotted in Section S.9 of the Supporting Information (Figure S.29 & S.30). The relevance of internal and external mass transfer limitations were probed with the Mears criterion [72] and the Weisz-Prater criterion [73], respectively (see Section S.10). It was determined that internal and external mass transfer rates were much faster than the observed experimental rates; thus, the kinetics were measured in the absence of mass transfer effects. In one example previously reported in a preceding publication [74], the coupling rate was transient over ~100 ks at a steady flow of reactants (Figure S.29). The sample was exposed

to the standard reaction condition and appeared to have reached a steady state rather quickly upon initial exposure to reaction conditions. However, after 50 ks, the coupling rate began to increase steadily over 60 ks (by ~2.5×) before appearing steady again. Negative order kinetics with respect to methanol were measured over the next ~200 ks and a persistent coupling rate increase (nearly twice the initial coupling rate) was observed upon return to the standard condition (Figure S.29). While the cause of this transient is unclear, it is likely this phenomenon results from alloy surface dynamics (i.e., restructuring) and slow accumulation (or depletion) of reactive surface intermediates.

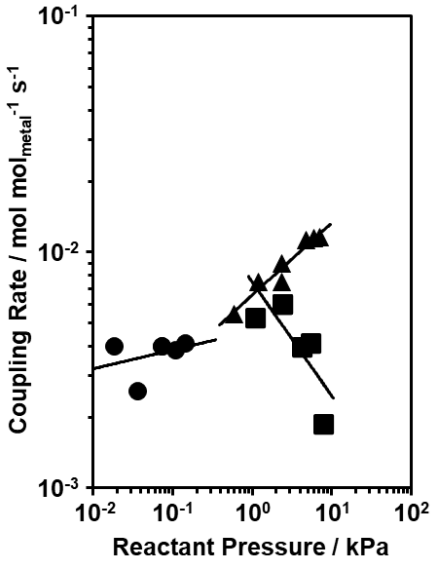

Figure 9. Reaction orders of methanol (squares), oxygen (triangles), and dimethylamine (circles). Reaction Conditions: 120 kPa (1.2-7.8 kPa methanol, 0.6-7.8 kPa O_2, 0.02-0.15 kPa DMA, 1.2 kPa CH_4 (internal standard), balance He), 398 K, 1:5 PdAu-Cs/SiO_2 mass; 0.0034 g diluted 6:1 w:w in Si-xerogel and sieved to 180 - 250μm. GHSV: 40000 hr^{-1}.

For kinetic measurements, the Cs-promoted catalyst was chosen for ease of keeping reactant conversion differential and because Cs has the largest ionic radius, lowest work function, lowest electronegativity, and other periodic trends that might result in the largest differences in apparent kinetics relative to an unpromoted catalyst. The comparatively lesser rate of the Cs-promoted catalyst allowed for rate increases due to bed temperature or reactant partial pressure while avoiding reaching mass-transfer-limited rates, which would have been likely for the K-promoted sample. Before measuring the apparent kinetics, both unpromoted and Cs-promoted catalysts were tested for DMF and H_2O product inhibition or promotion by co-feeding each in significant quantities compared to the amount of product produced under reaction conditions (50× and 25% of the water and the DMF formed from reaction, respectively). First, H_2O co-feed was examined as moisture has been previously reported to enhance oxygen activation and oxygen adatom mobility on Au and Au-based bimetallic surfaces [75-80]. Co-fed H_2O did not have any notable effect of rate on DMF formation (Figure S.37). However, TMU and MF rates both decreased (-34% and -53%, respectively) in the presence of co-fed H_2O (Figure S.40 & S.41). Since DMF is the major product (~70% carbon selectivity), the overall coupling rate was largely unaffected (Figure S.42). Given the extreme excess of H_2O (50× what is typically formed during reaction), it was concluded that the trace H_2O present in the methanol/DMA reactant solution and

the H_2O produced by reaction were irrelevant to the measured DMF rates and total coupling product rates, but that H_2O partial pressure was a considerable factor in the kinetics of TMU and MF production.

Once H_2O was determined to be kinetically irrelevant for the DMF and total coupling product rates, a 1 wt% DMF in H_2O solution was co-fed, which contributed 25% additional DMF above what forms in the absence of the co-feed. DMF was also determined to be kinetically irrelevant for the coupling product rate and carbon selectivity (Figure S.43). Under the 1 wt% DMF/H_2O co-feed, the TMU rate saw a similar decrease to that during the H_2O co-feed (Figure S.44). Thus, supplemental DMF was irrelevant for the TMU formation rates. It is surmised that DMF is not a reactive intermediate on the pathway for TMU formation. Unlike during the H_2O co-feed, the rate of MF was unaffected by the dilute DMF/H_2O co-feed, with no observable decrease in the presence of excess DMF and H_2O (Figure S.45). More detailed information on co-feed experiments is available in Section S.13 of the Supporting Information.

Next, apparent reaction orders for the reactants and the apparent activation energy were measured for 1:5 PdAu-Cs/SiO_2. Apparent reaction orders for DMF formation over the alkali-free sample were measured in a previous study [6] and were -0.48 ± 0.20, 0.43 ± 0.08, and 0.28 ± 0.02 with respect to methanol, DMA, and oxygen pressure [6]. Apparent reaction orders for 1:5 PdAu-Cs/SiO_2 were measured by the summation of the formation rates of all coupling products. The apparent reaction orders for 1:5 PdAu-Cs/SiO_2 were -0.27 ± 0.17, 0.04 ± 0.10, and 0.30 ± 0.05 with respect to methanol, DMA, and oxygen pressure (Figure 9, Table 4). The apparent reaction order plots for DMF, TMU, and MF individually can be found in the Supporting Information, Section S.14 (Figure S.47) and their individually measured reaction orders are listed in Table 4.

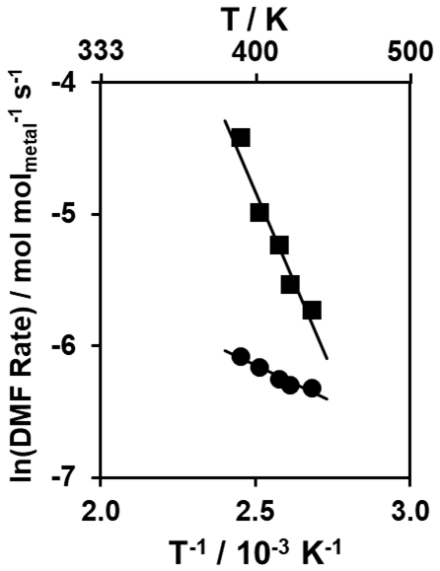

Figure 10. Arrhenius plots for the rate of DMF production as a function of temperature for 1:5 PdAu/SiO_2 (circles) and 1:5 PdAu-Cs/SiO_2 (squares). Reaction conditions: 120 kPa (2.4 kPa methanol, 1.2 kPa O_2, 0.07 kPa DMA, 1.2 kPa CH_4 (internal standard), balance He), 373-408 K, Catalyst mass: 1:5 PdAu/SiO_2: 0.0056 g diluted 6:1 w:w in Si-xerogel. 1:5 PdAu-Cs/SiO_2; 0.0034 g diluted 6:1 w:w in Si-xerogel. Catalyst powder sieved to 180 – 250 μm. GHSV of

The apparent activation energy for DMF formation was measured on 1:5 PdAu-Cs/SiO_2 for comparison to the alkali-free catalyst (Figure 10, Table 5). While the apparent activation energy

was low (9 ± 1 kJ mol^{-1}) for the alkali-free catalyst, the value increased to 45 ± 5 kJ mol^{-1} for the Cs-promoted sample (Figure 10). The activation energy for the sum of the formation rates of all coupling products was 27 ± 3 kJ mol^{-1} (Figure S.48) and the apparent activation energies for DMF, TMU, and MF individually are displayed in Figure S.49. Interestingly, the value of 45 ± 5 kJ mol^{-1} was similar in magnitude to the previous values measured for this reaction on $PdAu/SiO_2$ with larger surface-weighted average particle diameters and nanoporous gold (54 ± 3 kJ mol^{-1}) [5].

The increase in the reaction rate concurrent with an increase in apparent activation suggests that the pre-exponential factor (*A*) increases due either to changes in apparent reaction entropy change of reaction, or to an increase in the number of active sites upon Cs promotion. The trend lines depicted in Figure 10 can be extrapolated to their y-intercepts to determine pre-exponential factors (*A*). 1:5 $PdAu/SiO_2$ has a value of *A* of 0.034 mol mol_{metal}^{-1} s^{-1} and 1:5 $PdAu\text{-}Cs/SiO_2$ is 9.18 mol mol_{metal}^{-1} s^{-1}. For these $PdAu/SiO_2$ catalysts, we cannot distinguish between a change in mechanism and a change in the number of active sites, but it is plausible that the surface has a higher density of active sites that follow a reaction pathway with a higher apparent energy barrier. It is possible that the increased apparent activation energy over the Cs-promoted sample results from an increase in the coverage of DMA on the surface, reflected in a near zero apparent reaction order with respect to DMA pressure for the Cs-promoted sample, and an apparent reaction order of ~0.4 for the alkali-free sample.

Table 4. Apparent reaction orders for formation of DMF, TMU, MF and the sum of all coupling products with respect to each reactant on 1:5 $PdAu\text{-}Cs/SiO_2$

		Reactant		
		Methanol	**DMA**	**O_2**
Product	**DMF**	-0.47 ± 0.19	0.08 ± 0.11	0.31 ± 0.04
	TMU	-0.84 ± 0.19	0.12 ± 0.15	0.02 ± 0.34
	MF	0.46 ± 0.22	-0.21 ± 0.13	0.32 ± 0.06
	Sum of Coupling Products	-0.27 ± 0.17	0.04 ± 0.10	0.30 ± 0.05

Table 5. Apparent activation energies for formation of DMF, TMU, MF and the sum of all coupling products on 1:5 $PdAu\text{-}Cs/SiO_2$

Product	**DMF**	45 ± 5 kJ mol^{-1}
	TMU	28 ± 6 kJ mol^{-1}
	MF	71 ± 6 kJ mol^{-1}
	Sum of Coupling Products	27 ± 3 kJ mol^{-1}

3.5 Economic Feasibility of Promoted $PdAu/SiO_2$ Catalysts for Oxidative Coupling

Three different $PdAu/SiO_2$ catalysts tested for the oxidative coupling of methanol and dimethylamine at a similar reaction condition are compared in Figure 11. The left bar represents the DMF rate from $PdAu/SiO_2$ synthesized with colloidal methods (adapted from Liu et al. [81], named "1:10 $PdAu/SiO_2$-colloidal" herein). The 1:10 $PdAu/SiO_2$-colloidal catalyst was tested in our previous study of alcohol-amine cross coupling reactions catalyzed by bimetallic alloys [5]. TEM images of the 1:10 $PdAu/SiO_2$-colloidal sample revealed an average surface-weighted particle diameter of 23 ± 8 nm, and its steady state rate of DMF formation was $3.5 \cdot 10^{-8}$ mol g_{cat}^{-1} s^{-1} [5]. A subsequent investigation using SEA synthesis allowed for small particle sizes of 4.4 ± 1

nm which in turn increased rates and selectivity of DMF formation with a sample of a similar Pd:Au ratio (named "1:10 PdAu/SiO_2-SEA" herein) [6].

The steady state rate of DMF formation over 1:10 PdAu/SiO_2-SEA is shown as the center bar in Figure 11. Finally, the righthand bar in Figure 11 shows the coupling rate over the most reactive catalyst from this study (1:5 PdAu-K/SiO_2). The "Window of Useful Catalytic Activity" as defined by Weisz [82] is shown by the dashed horizontal lines encompassing the shaded area. Weisz defined the lower boundary as the minimum rate per volume of a reactor a catalyst should give to be economically viable, while above the upper boundary is where catalytic activity is fast enough to induce mass and heat transfer limitations [82]. This suggests that the 1:5 PdAu-K/SiO_2 catalyst reported in this work could be an industrially practical catalyst for large-scale continuous flow oxidative coupling reactions in packed bed reactors.

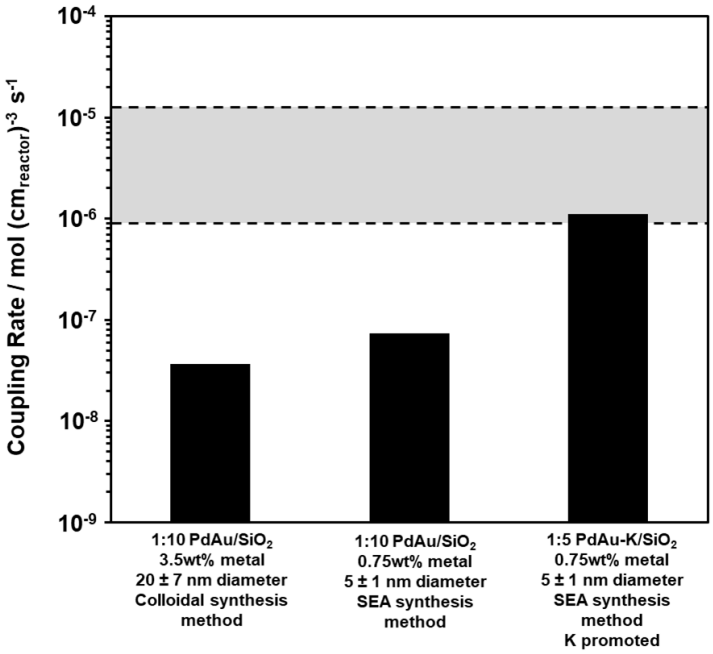

Figure 11. Comparison of catalysts from previous studies [5, 6] and the most reactive catalyst presented here with guidelines (grey area) from Weisz [82]. Assumes a catalyst bed density of 1 g cm^{-1}. Reaction conditions: 120 kPa (2.4 kPa methanol, 1.2 kPa O_2, 0.07 kPa DMA, 1.2 kPa CH_4 (internal standard), balance He), 398 K, catalyst mass: 0.0043-0.0214 g diluted in Si-xerogel and sieved to 180–250 μm. GHSV of 40000 hr^{-1}.

Conclusions

As established in our previous work [6], PdAu/SiO_2 catalysts synthesized by SEA catalyze the oxidative coupling of methanol and DMA; the alkali-free catalyst with a Pd:Au ratio of 1:5 formed DMF with ~95% carbon selectivity at a rate of $2.0 \cdot 10^{-3}$ mol mol$_{metal}^{-1}$ s^{-1}. When the SEA procedure was repeated but pH control was facilitated by an alkali hydroxide salt instead of NH_4OH, uptake of the alkali ion from the synthesis solution onto the deprotonated silica surface occured. The amount of alkali species adsorbed varies with the alkali identity despite near-identical synthesis conditions. The presence of the alkali metals influences the oxidative coupling of methanol and DMA on PdAu nanoparticles by increasing the coupling rate and altering the coupling selectivity. In the presence of Li, TMU forms in addition to DMF, and TMU has 29%

carbon selectivity. The presence of Na, K, or Cs on the catalyst also induces the formation of TMU and MF. While alkali promoters increase the rate of CO_2 formation, the CO_2 carbon selectivity never exceeds 5%, similar to an alkali-free 1:5 PdAu/SiO_2 catalyst. The rate of oxidative coupling promotion is unpromoted < Li < Na < Cs < K, with K exhibiting a 12.5× increase in coupling rate relative to the alkali-free catalyst.

The apparent kinetics for the sum of all coupling products with respect to each reactant were compared between an unpromoted 1:5 PdAu/SiO_2 and a Cs-promoted 1:5 PdAu/SiO_2 catalyst. The apparent reaction order with respect to O_2 was unaffected by the Cs, while the apparent reaction order with respect to DMA changed from 0.4 ± 0.1 on the alkali-free catalyst to zero order over the Cs-promoted 1:5 PdAu/SiO_2 catalyst. The apparent activation energy with respect to DMF formation increased from 9 ± 1 kJ mol^{-1} to 45 ± 5 kJ mol^{-1} upon the introduction of Cs. This study demonstrates that the presence of alkali metals introduced during synthesis of PdAu/SiO_2 greatly effects the rate and selectivity of the oxidative coupling of methanol and DMA, and that kinetic differences between unpromoted and promoted catalysts suggest the alkali metals influence the coverages or mechanisms of the surface reaction. This study presents the opportunity for facile synthesis of alkali-promoted metal catalysts prepared by SEA beyond PdAu/SiO_2 by simply varying the identity of the base used for pH control during the synthesis.

CReDiT Authorship Contribution Statement

Alexander P. Minne: Writing – review & editing, Writing – original draft, formal analysis, data collection and curation. **Treycen D. Garton:** Writing – review & editing, Writing – original draft, catalyst synthesis, introduction. **Ethan P. Iaia:** Writing – review & editing, original draft, XAS data collection and analysis. **Eli Stavitski:** Writing – review & editing, XAS data collection and analysis. **James W. Harris:** Writing – review & editing, Writing – original draft, project administration, funding acquisition, data curation, conceptualization.

Declaration of Competing Interest

The authors have no competing interests to disclose.

Acknowledgements

The authors acknowledge Alabama Materials Institute for access to TEM and XRD, and funding support from ACS PRF award no. 65488-DNI5. This research used resource beamline 8-ID of the National Synchrotron Light Source II, a U.S. Department of Energy (DOE) Office of Science User Facility operated for the DOE Office of Science by Brookhaven National Laboratory under Contract No. DE-SC0012704. Use of the Stanford Synchrotron Radiation Lightsource, SLAC National Accelerator Laboratory, is supported by the U.S. Department of Energy, Office of Science, Office of Basic Energy Sciences under Contract No. DE-AC02-76SF00515. The authors acknowledge Drs. Denis Leshchev and Dominik Wierzbicki of BNL and Drs. Simon Bare, Adam Hoffman, Jorge Perez-Aguilar, and Jiyun Hong of SSRL for assistance at respective beamlines.

Appendix A. Supplementary material

The supplementary material includes process flow diagram, N_2 isotherms, XRD patterns, additional XAS spectra, time on stream data, supplemental calculations, co-feed information, and additional plots of comparison, and plots of kinetic data.

References

[1] A. Filie, T. Shirman, A.C. Foucher, E.A. Stach, M. Aizenburg, J. Aizenburg, C.M. Friend, R.J. Madix, Dilute Pd-in-Au alloy RCT-SiO2 catalysts for enhanced oxidative methanol coupling, Journal of Catalysis, 404 (2021) 943-953.
[2] J.D. Lee, A. Filie, L. Wilson, Nguyen, T. Shirman, E. Guan, M. Luneau, M. Aizenberg, M. Aizenberg, R.J. Madix, C.M. Friend, Selective oxidation of linear alcohols: the promotional effect of water and inhibiting effect of carboxylates over dilute PdAu catalysts, Journal of Materials Chemistry A, 12 (2024) 13778-13791
[3] G.T. Whiting, S.A. Kondrat, C. Hammond, N. Dimitratos, H. He, D.J. Morgan, N.F. Dummer, J.K. Bartley, C.J. Kiely, S.H. Taylor, G.J. Hutchings, Methyl Formate Formation from Methanol Oxidation Using Supported Gold–Palladium Nanoparticles, ACS Catalysis, 5 (2015) 637-644.
[4] J.-b. Wu, R.-p. Shi, Z.-f. Qin, H. Liu, Z.-k. Li, H.-q. Zhu, Y.-x. Zhao, J.-g. Wang, Selective oxidation of methanol to methyl formate over bimetallic Au-Pd nanoparticles supported on SiO2, Journal of Fuel Chemistry and Technology, 47 (2019) 780-790.
[5] A.P. Minne, T. Maxson, T. Szilvási, J.W. Harris, Selective vapor-phase formation of dimethylformamide via oxidative coupling of methanol and dimethylamine over bimetallic catalysts, Catal. Sci. Technol., 14 (2024) 1534-1549.
[6] A.P. Minne, E.P. Iaia, E. Stavitski, J.W. Harris, Impact of Particle Size on the Vapor-Phase Oxidative Coupling of Methanol and Dimethylamine over Palladium–Gold Nanoparticles, ACS Catalysis, (2024) 17209-17225.
[7] G.J. Hutchings, Promotion in Heterogeneous Catalysis: A Topic Requiring a New Approach?, Catalysis Letters, 75 (2001) 1-12.
[8] A.P. Raje, R.J. O'Brien, B.H. Davis, Effect of Potassium Promotion on Iron-Based Catalysts for Fischer–Tropsch Synthesis, Journal of Catalysis, 180 (1998) 36-43.
[9] J. Nakamura, J.M. Campbell, C.T. Campbell, Kinetics and mechanism of the water-gas shift reaction catalysed by the clean and Cs-promoted Cu(110) surface: a comparison with Cu(111), J. Chem. Soc., Faraday Trans., 86 (1990) 2725-2734.
[10] A. Dong, A. Shakouri, S. Karakalos, D. Blom, C.T. Williams, R. J.R., The preparation of silica supported, dilute limit PdAu alloys via simultaneous strong electrostatic adsorption, Catal. Sci. Technol., 13 (2023) 3020-3034.
[11] A.U. Ojo, D. Shakya, J. Stetzler, M. Gbadamosi, R.M. Masudur, N. Acharya, N. Thornburg, J. Tengco, S.K. Balijepalli, J.R. Monnier, D.A. Chen, J.R. Regalbuto, The enhanced reactivity of graphitic supports for Pd catalyzed toluene hydrogenation, Journal of Catalysis, 445 (2025) 116029.
[12] M.F. Patwary, M. Neito, A.U. Ojo, J.R. Regalbuto, The Effect of Reduction Pretreatments on the Size of Supported Pt and Pd Nanoparticles Prepared by Strong Electrostatic Adsorption, Catal Lett, 154 (2024) 4352-4366.
[13] S.R. Noble, S.E. Barnes, R. Banerjee, J. Miller, J.R. Regalbuto, Supported nanoparticle synthesis with Au bis-Ethylenediamine: The mechanism of adsorption onto oxides and carbons, Journal of Catalysis, 393 (2021) 344-356.
[14] H.-R. Cho, J.R. Regalbuto, The rational synthesis of Pt-Pd bimetallic catalysts by electrostatic adsorption, Catalysis Today, 246 (2015) 143-153.
[15] L. Jiao, J.R. Regalbuto, The synthesis of highly dispersed noble and base metals on silica via strong electrostatic adsorption: I. Amorphous silica, Journal of Catalysis, 260 (2008) 329-341.

[16] M. Schreier, J.R. Regalbuto, A fundamental study of Pt tetraammine impregnation of silica: 1. The electrostatic nature of platinum adsorption, Journal of Catalysis, 225 (2004) 190-202.
[17] B. Mirkelamoglu, G. Karakas, The role of alkali-metal promotion on CO oxidation over PdO/SnO2 catalysts, Applied Catalysis A: General, 299 (2006) 84-94.
[18] Y. Li, C. Zhang, H. He, J. Zhang, M. Chen, Influence of alkali metals on Pd/TiO2 catalysts for catalytic oxidation of formaldehyde at room temperature, Catal. Sci. Technol., 6 (2016) 2289-2295.
[19] N. Macleod, J. Isaac, R.M. Lambert, Sodium Promotion of Pd/γ-Al2O3 Catalysts Operated under Simulated "Three-Way" Conditions, Journal of Catalysis, 198 (2001) 128-135.
[20] S.J. Pratt, D.A. King, Coverage dependent promoter action: K coadsorption and reactions with CO and CO2 on Pd{1 1 0}, Surface Science, 540 (2003) 185-206.
[21] H. Tanaka, S.-i. Ito, S. Kameoka, K. Tomishige, K. Kunimori, Catalytic performance of K-promoted Rh/USY catalysts in preferential oxidation of CO in rich hydrogen, Applied Catalysis A: General, 250 (2003) 255-263.
[22] H.B. Michaelson, The work function of the elements and its periodicity, Journal of Applied Physics, 48 (1977) 4729-4733.
[23] J. Hölzl, F.K. Schilte, Work function of metals, in: J. Hölzl, F.K. Schilte, H. Wagner (Eds.) Solid Surface Physics, Springer, Berlin, Heidelberg, 1979, pp. 1-150.
[24] W.M. Haynes, D.R. Lide, T.J. Bruno, CRC Handbook of Chemistry and Physics, CRC Press, 2014.
[25] C.G. Vayenas, S. Bebelis, C. Pliangoes, S. Brosda, D. Triplakides, Electrochemical Activation of Catalysis: Promotion, Electrochemical Promotion, and Metal-Support Interactions., Kluwer Academic Publishers, New York, New York, 2002, pp. 15-82.
[26] A. Farkas, F. Solymosi, Photolysis of the CO2 + K/Au(111) System, The Journal of Physical Chemistry C, 114 (2010) 16979-16982.
[27] R.J. Behm, D.K. Flynn, K.D. Jamison, G. Ertl, P.A. Thiel, Structure and mechanism of alkali-metal-induced reconstruction of fcc (110) surfaces, Phys. Rev. B, 36 (1987) 9267-9270.
[28] P. Häberle, T. Gustafsson, Medium-energy ion-scattering analysis of the c(2×2) structure induced by K on Au(110), Phys. Rev. B, 40 (1989) 8218-8224.
[29] J.V. Barth, R. Schuster, J. Wintterlin, R.J. Behm, G. Ertl, Scanning-tunneling-microscopy observation of K-induced reconstructions on Au(110), Phys. Rev. B, 51 (1995) 4402-4414.
[30] A. Neumann, S.L.M. Schroeder, K. Christmann, Adsorption of sodium and potassium on a gold(100) surface: An example of alkali-metal-induced deconstruction, Phys. Rev. B, 51 (1995) 17007-17022.
[31] H. Tochihara, S. Mizuno, Composite surface structures formed by restructuring-type adsorption of alkali-metals on fcc metals, Progress in Surface Science, 58 (1998) 1-74.
[32] M. Okada, H. Iwai, R. Klauser, Y. Murata, Potassium-induced restructuring of the Au(001) surface, Journal of Physics: Condensed Matter, 4 (1992) L593.
[33] S.L.M. Schroeder, A. Neumann, T. Solomun, P. Lenz-Solomun, K. Christmann, Potassium-induced reconstructive phase transitions on Au(100), Surface Science, 337 (1995) 285-293.
[34] J.V. Barth, R. Schuster, R.J. Behm, G. Ertl, K-induced restructuring of Au(001) observed by scanning tunneling microscopy, Surface Science, 302 (1994) 158-170.
[35] J.V. Barth, R.J. Behm, G. Ertl, Adsorption, surface restructuring and alloy formation in the Na/Au(111) system, Surface Science, 341 (1995) 62-91.
[36] J.V. Barth, R.J. Behm, G. Ertl, Mesoscopic structural transformations of the Au(111) surface induced by alkali metal adsorption, Surface Science, 302 (1994) L319-L324.

[37] J.V. Barth, H. Brune, R. Schuster, G. Ertl, R.J. Behm, Intermixing and two-dimensional alloy formation in the Na/Au(111) system, Surface Science, 292 (1993) L769-L774.
[38] J. Ren, Y. Wang, J. Zhao, S. Tan, H. Petek, K Atom Promotion of O2 Chemisorption on Au(111) Surface, Journal of the American Chemical Society, 141 (2019) 4438-4444.
[39] R. Van Grieken, C. Martos, M. Sánchez-Sánchez, D.P. Serrano, J.A. Melero, J. Iglesias, A.G. Cubero, Synthesis of Sn–silicalite from hydrothermal conversion of SiO2–SnO2 xerogels, Microporous and Mesoporous Materials, 119 (2009) 176-185.
[40] B.P. Block, J.C. Bailar, The Reaction of Gold(III) with Some Bidentate Coördinating Groups, Journal of the American Chemical Society, 73 (1951) 4722-4725.
[41] S.R. Bare, A. Boubnov, J. Hong, A.S. Hoffman, The Consortium for Operando and Advanced Catalyst Characterization via Electronic Spectroscopy and Structure (Co-ACCESS) at Stanford Synchrotron Radiation Lightsource (SSRL), Synchrotron Radiation News, 33 (2020) 15-19.
[42] B. Ravel, M. Newville, ATHENA, ARTEMIS, HEPHAESTUS: data analysis for X-ray absorption spectroscopy using IFEFFIT, J Synchrotron Rad, 12 (2005) 537-541.
[43] A. Jain, S.P. Ong, G. Hautier, W. Chen, W.D. Richards, S. Dacek, S. Cholia, D. Gunter, D. Skinner, G. Ceder, K. Persson, Commentary: The Materials Project: A materials genome approach to accelerating materials innovation, APL Materials, 1 (2013) 011002.
[44] D. Leshchev, M. Rakitin, B. Luvizotto, R. Kadyrov, B. Ravel, K. Attenkofer, E. Stavitski, The Inner Shell Spectroscopy beamline at NSLS-II: a facility for in situ and operando X-ray absorption spectroscopy for materials research, J Synchrotron Rad, 29 (2022) 1095-1106.
[45] G. Bergeret, P. Gallezot, Particle Size and Dispersion Measurements, Handbook of Heterogeneous Catalysis, John Wiley & Sons, Ltd2008, pp. 738-765.
[46] S. Goel, S.I. Zones, E. Iglesia, Encapsulation of Metal Clusters within MFI via Interzeolite Transformations and Direct Hydrothermal Syntheses and Catalytic Consequences of Their Confinement, Journal of the American Chemical Society, 136 (2014) 15280-15290.
[47] M.P. Perich, C.R. O'Conner, K.M. Draijer, N.L. Visser, N. Artrith, C. Reece, P.E.d. Jongh, J.E.S. van der Hoeven, In situ analysis of gas dependent redistribution kinetics in bimetallic Au-Pd nanoparticles, Journal of Materials Chemistry A, 12 (2024) 32760-32774.
[48] M. Luneau, E. Guan, W. Chen, A.C. Foucher, N. Marcella, T. Shirman, D.M.A. Berbart, J. Aizenburg, M. Aizenburg, E.A. Stach, R.J. Madix, A.I. Frenkel, C.M. Friend, Enhancing catalytic performance of dilute metal alloy nanomaterials, Communications Chemistry, 3 (2020) 1-9.
[49] A. Galarneau, F. Villemot, J. Rodriguez, F. Fajula, B. Coasne, Validity of the t-plot Method to Assess Microporosity in Hierarchical Micro/Mesoporous Materials, Langmuir, 30 (2014) 13266-13274.
[50] L. Luo, S. Wang, C. Fan, L. Yang, Z. Wu, Z. Qin, H. Zhu, W. Fan, J. Wang, Promoting effect of alkali metal cations on the catalytic performance of Pd/H-ZSM-5 in the combustion of lean methane, Applied Catalysis A: General, 602 (2020) 117678.
[51] S.S. Mulla, N. Chen, L. Cumaranatunge, W.N. Delgass, W.S. Epling, F.H. Ribeiro, Effect of potassium and water vapor on the catalytic reaction of nitric oxide and dioxygen over platinum, Catalysis Today, 114 (2006) 57-63.
[52] Y. Zhai, D. Pierre, R. Si, W. Deng, P. Ferrin, A.U. Nilekar, G. Peng, J.A. Herron, D.C. Bell, H. Saltsburg, M. Mavrikakis, M. Flytzani-Stephanopoulos, Alkali-Stabilized Pt-OHx Species Catalyze Low-Temperature Water-Gas Shift Reactions, Science, 329 (2010) 1633-1636.

[53] M. Yang, S. Li, Y. Wang, J.A. Herron, Y. Xu, L.F. Allard, S. Lee, J. Huang, M. Mavrikakis, M. Flytzani-Stephanopoulos, Catalytically active Au-O(OH)x- species stabilized by alkali ions on zeolites and mesoporous oxides, Science, 346 (2014) 1498-1501.
[54] H. Liu, J. Liang, J. Li, Y. Du, H. Chen, C. Du, L. Wang, Y. Li, Y. Huang, D. Chen, Exploration of Alkali Metal-Induced Effects on Promoting Ammonia Decomposition Performance, Energy & Fuels, 38 (2024) 13255-13263.
[55] A. Boubnov, J. Timoshenko, C.J. Wrasman, A.S. Hoffman, M. Cargnello, A.I. Frenkel, S.R. Bare, Insight into restructuring of Pd-Au nanoparticles using EXAFS, Radiation Physics and Chemistry, 175 (2020) 108304.
[56] R.S. McDonald, Surface Functionality of Amorphous Silica by Infrared Spectroscopy, The Journal of Physical Chemistry, 62 (1958) 1168-1178.
[57] A. Díaz, D.R. Acosta, J.A. Odriozola, M. Montes, Characterization of Alkali-Doped Ni/SiO2 Catalysts, J. Phys. Chem. B, 101 (1997) 1782-1790.
[58] Y. Marcus, Thermodynamics of Solvation of Ions, J. CHEM. SOC. FARADAY TRANS., 87 (1991) 2995-2999.
[59] H. Park, C. Li, P.A. Kohl, Performance of Anion Exchange Membrane Water Electrolysis with High Ionic Strength Electrolyte, J. Electrochem. Soc., 171 (2024) 024506.
[60] R. Wang, Z. Wu, C. Chen, Z. Qin, H. Zhu, G. Wang, H. Wu, W. Dong, W. Fan, J. Wang, Graphene-supported Au–Pd bimetallic nanoparticles with excellent catalytic performance in selective oxidation of methanol to methyl formate, Chemical Communications, 49 (2013) 8250-8252.
[61] D. Shi, J. Liu, R. Sun, S. Ji, S.M. Rogers, B.M. Connolly, N. Dimitratos, A.E.H. Wheatley, Preparation of bifunctional Au-Pd/TiO2 catalysts and research on methanol liquid phase one-step oxidation to methyl formate, Catalysis Today, 316 (2018) 206-213.
[62] B. Xu, L. Zhou, R.J. Madix, C.M. Friend, Highly Selective Acylation of Dimethylamine Mediated by Oxygen Atoms on Metallic Gold Surfaces, Angewandte Chemie, 49 (2010) 394-398.
[63] A. Wichmann, M. Baumer, A. Wittstock, Oxidative Coupling of Alcohols and Amines over Bimetallic Unsupported Nanoporous Gold: Tailored Activity through Mechanistic Predictability, ChemCatChem, 7 (2014) 70-74.
[64] C.T. Campbell, Bimetallic Surface Chemistry, Annual Review of Physical Chemistry, 41 (1990) 775-837.
[65] H.P. Bonzel, Alkali-promoted gas adsorption and surface reactions on metals, Journal of Vacuum Science & Technology A, 2 (1984) 866-872.
[66] A. Wong, Q. Liu, S. Griffin, A. Nichills, J.R. Regalbuto, Synthesis of ultrasmall, homogeneously alloyed, bimetallic nanoparticles on silica supports, Science, 358 (2017) 1427-1430.
[67] N. Gong, R. Zhou, H. Wan, H. Hou, X. Dou, J. Gong, H. P., L. Liu, Tuning the Selectivity in the Nonoxidative Alkane Dehydrogenation Reaction by Potassium-Promoted Zeolite-Encapsulated Pt Catalysts, JACS Au, 4 (2024) 4934-4947.
[68] H. Chen, K. Zhang, Z. Feng, L. Chen, Y. Zhang, Q. Zhang, B. Peng, D. Li, Y. Tian, R. Huang, Z. Li, Construction of Pd@K-Silicalite-1 via in situ encapsulation and alkali metal modification for catalytic elimination of formaldehyde at room temperature, Separation and Purification Technology, 341 (2024) 126889.
[69] S. Cao, Y. Zhao, S. Lee, S. Yang, J. Liu, G. Giannakakis, M. Li, M. Ouyang, D. Wang, C. Sykes, M. Flytzani-Stephanopoulos, High-loading single Pt atom sites [Pt-O(OH)x] catalyze the

CO PROX reaction with high activity and selectivity at mild conditions, Science Advances, 6 (2020).
[70] J.A. Rodriguez, D. Grinter, P. Ramírez, D.J. Stacchiola, S. Senanayake, High Activity of Au/K/TiO2(110) for CO Oxidation: Alkali-Metal-Enhanced Dispersion of Au and Bonding of CO, The Journal of Physical Chemistry C, 122 (2018) 4324-4330.
[71] J. Gong, Structure and Surface Chemistry of Gold-Based Model Catalysts, Chemical Reviews, 112 (2012) 2987-3054.
[72] D.E. Mears, Tests for Transport Limitations in Experimental Catalytic Reactors, Industrial & Engineering Chemistry Process Design and Development, 10 (1971) 541-547.
[73] P.B. Weisz, C.D. Prater, Interpretation of Measurements in Experimental Catalysis, in: W.G. Frenkenburg, V.I. Komarewsky, E.K. Rideal (Eds.) Advances in Catalysis, Academic Press1954, pp. 143-196.
[74] S.N. Borate, A.P. Minne, J.W. Harris, Extracting value from transients observed during measurement of steady-state kinetics, Journal of Catalysis, 443 (2025) 115975.
[75] W. Dononelli, G. Tomaschun, T. Klüner, L.V. Moskaleva, Understanding Oxygen Activation on Nanoporous Gold, ACS Catalysis, 9 (2019) 5204-5216.
[76] B.N. Zope, D.D. Hibbitts, M. Neurock, R.J. Davis, Reactivity of the Gold/Water Interface During Selective Oxidation Catalysis, Science, 330 (2010) 74-78.
[77] T. Fujitani, I. Nakamura, M. Haruta, Role of Water in CO Oxidation on Gold Catalysts, Catal Lett, 144 (2014) 1475-1486.
[78] J. Saavedra, H.A. Doan, C.J. Pursell, L.C. Grabow, B.D. Chandler, The critical role of water at the gold-titania interface in catalytic CO oxidation, Science, 345 (2014) 1599-1602.
[79] F. Xu, I. Fampiou, C.R. O'Connor, S. Karakalos, F. Hiebel, E. Kaxiras, R.J. Madix, C.M. Friend, Water facilitates oxygen migration on gold surfaces, Phys. Chem. Chem. Phys., 20 (2018) 2196-2204.
[80] L. Mastroianni, T. Weckman, K. Eränen, V. Russo, D.Y. Murzin, K. Honkala, T. Salmi, Oxidative dehydrogenation of alcohols on gold: An experimental and computational study on the role of water and the alcohol chain length, Journal of Catalysis, 425 (2023) 233-244.
[81] J. Liu, J. Shan, F.R. Lucci, S. Cao, C. Sykes, M. Flytzani-Stephanopoulos, Palladium–gold single atom alloy catalysts for liquid phase selective hydrogenation of 1-hexyne, Catal. Sci. Technol., 7 (2017) 4276-4284.
[82] P.B. Weisz, The Science of the Possible, CHEMTECH, 12 (1982) 424-425.